Available online at www.sciencedirect.com
ScienceDirect
Comput. Methods Appl. Mech. Engrg. 384 (2021) 114000
Computer methods in applied mechanics and engineering
www.elsevier.com/locate/cma

On the design of multimaterial structural topologies using Integer Programming

Raghavendra Sivapuram[a,*], Renato Picelli[b], Gil Ho Yoon[c], Bing Yi[d]

[a] *Structural Engineering, University of California San Diego, La Jolla, CA 92093, USA*
[b] *Department of Mining and Petroleum Engineering, University of São Paulo, Praca Narçiso de Andrade s/n, Vila Mathias, Santos - SP, 11013-560, Brazil*
[c] *School of Mechanical Engineering, Hanyang University, Seoul, South Korea*
[d] *School of Traffic and Transportation Engineering, Central South University, Changsha, China*

Received 9 November 2020; received in revised form 29 May 2021; accepted 10 June 2021
Available online 23 June 2021

Abstract

This paper presents a framework for the discrete design of optimal multimaterial structural topologies using integer design variables and mathematical programming. The structural optimization problems: compliance minimization subject to mass constraint, and mass minimization subject to compliance constraint are used to design the multimaterial topologies in this work. The extended SIMP interpolation is used to interpolate the different materials available for structural design, and the material phases in each element are represented using binary design variables, one variable per available material. The Topology Optimization of Binary Structure (TOBS) method (Sivapuram and Picelli, 2018) is employed, wherein the nonlinear objective/constraint functions of optimization are sequentially approximated (herein, linearized) to obtain a sequence of Integer Linear Programs (ILPs). A novel truncation error-regulating constraint in terms of the Young's moduli of the elements is introduced to maintain the sequential approximations valid, by restricting large changes in successive structural topologies. A commercial branch-and-bound solver is used to solve the integer subproblems yielding perfectly binary solutions which guarantee discrete structural topologies with clear material interfaces at each iteration. Adjoint sensitivities are computed to generate the integer subproblems, and the sensitivities are filtered using a conventional mesh-independent sensitivity filter. Few examples show the design of multimaterial structures in the presence of design-dependent loads: hydrostatic pressure loads and self-weight loads. This work also demonstrates through few examples, convergence of optimal multimaterial topologies at inactive constraint values when different type of loadings simultaneously act on the structure.

Keywords: Multimaterial; Extended SIMP; Binary variables; Truncation error; Pressure loads; Inactive constraint

1. Introduction

The engineering world continuously strives to develop methodologies which aid in the design of effective and light-weight structures. Topology optimization is one such numerical method which enables to design optimally performing structural topologies. [1] used the numerical homogenization method to design structures made of single

* Corresponding author.
E-mail address: rsivapur@eng.ucsd.edu (R. Sivapuram).

https://doi.org/10.1016/j.cma.2021.114000

material in their pioneering work of topology optimization. Several works followed exploring topology optimization for the design of structures in different applications considering a variety of performance measures and constraints. It is vital to have a robust formulation to design complex optimal structures, especially when using multiphysics, design-dependent loads, etc. The rapid growth in the additive manufacturing of structures makes the complex designs obtained through structural optimization very practical [2].

Multimaterial structural optimization unlocks the capability to design even more efficient and high-performing structures because of the increased design space. The material at each point in the structure can be chosen optimally according to performance requirements whilst maintaining the structure light-weight. The multimaterial structures obtained through structural optimization can be manufactured through additive manufacturing techniques [2,3]. Multiscale optimization is similar to multimaterial optimization in that it involves the design of architected material (can use single [4] or multiple [5] base materials) at each point in the design domain.

One of the first works in multimaterial optimization designed microstructures with extreme material properties like thermal expansion coefficient [6]. They used an extended SIMP (Solid Isotropic Material with Penalization) interpolation for the material properties which is described in the later sections. The same interpolation is used in [7] to design multimaterial microstructures with extreme bulk moduli. The extended SIMP interpolation is just a recursive form of the original SIMP interpolation for single materials [8], and so is also called Recursive Multiphase Material Interpolation (RMMI) [9]. Homogenization-based structural optimization was used in [10] to design optimized multimaterial macrostructures. The interpolation of Hashin–Shtrikman bounds of the material properties was used in [11] to design bi-material thermal actuators. Most methods in multimaterial structural optimization use additional design variables over single material optimization for properly defining the material located at each point in the design domain. A peak function-based material interpolation [12] can be used to avoid adding additional design variables in multimaterial optimization by using smoothened versions of the Kronecker delta functions defining the material phase at any point in the structure. In the level-set methods, a “color”-based level-set method was used for the design of optimal multimaterial macrostructures by using very few level-set functions to represent multimaterial geometries [13]. Using the same level-set framework, [14] optimized for multimaterial force inverters and other compliant mechanisms. However, the optimal topologies include redundant material phases when the number of material phases available is not a power of 2, which requires special interpretations. Optimal multimaterial piezoelectric actuators are designed in [15] using a multiphase level-set method of piece-wise constants. A different material interpolation scheme for multimaterial optimization is proposed in [16], called Discrete Material Optimization (DMO) advantageous when several candidate materials are available for optimization. DMO is used in [17] for the design of optimal multimaterial composite shell structures considering buckling. Owing to the uniformity of weights in the interpolation of material properties, DMO is also called Uniform Multiphase Material Interpolation (UMMI) [9]. DMO allows for a linear form of mass constraint which is beneficial for convex programming methods. The UMMI scheme was used for the design of optimal multimaterial thermoelastic structures in [18] in the presence of a linear mass constraint. An ordered SIMP interpolation was proposed in [19] which uses one design variable per element, regardless of the number of candidate materials. However, the interpolated material properties are not differentiable when any element is made of one of the candidate materials.

Bidirectional Evolutionary Structural Optimization (BESO) was first used for multimaterial optimization in [20] with two candidate materials for compliance minimization in the presence of volume constraints. BESO was used in multimaterial optimization considering interval loading uncertainty in [21], again in the presence of volume constraints. Conventional BESO method requires volume constraint for design variable update, and so problems involving no volume constraint are nontrivial to solve [22,23]. An efficient MATLAB code for multimaterial structural optimization is presented in [24] using the ZPR (Zhang–Paulino–Ramos Jr.) design variable update scheme considering polyhedral finite elements and many volume constraints. An improved ZPR update scheme is applied to thermomechanical problems in [25] whilst controlling the complexity of the topologies and length scale of the associated support structures used in the additive manufacturing. A Moving Morphable Component (MMC) approach is used in [26] for multimaterial optimization under volume constraints where the optimization starts with defining an initial solution consisting of components with uniform material properties.

Obtaining optimal structural topologies with clear boundaries is of pivotal importance in manufacturing and in dealing with design-dependent loads. The structural optimization methods like SIMP [8] pose an uncertainty in the structural boundary because of the use of continuous density variables. Special post-processing techniques can be

employed to obtain an estimate for the structural boundary after optimization [27–29]. The SIMP method is also known to yield optimized solutions with too many intermediate densities when multiple physics are involved in the problem [30]. In the multimaterial scenario, not only the structural boundary, but all the material interfaces are fuzzy, which leads to difficulties in considering material interface effect in the structural analysis [31]. [31] developed an extended two-step filtering approach to approximately construct the multi-material interfaces. The level-set based structural optimization techniques employ a level-set function to implicitly define the structural boundary [32–34]. The classical SIMP method is also known to exhibit parasitic effects for low densities due to the incorrect modeling of effective mechanical and mass properties in the vicinity of zero density [35]. The level-set function is defined at a set of grid points, and the structural boundary is only defined approximately using linear interpolation [33], whereas the level-set function is a rational function. The level-set method also involves intricate numerical machinery to stabilize the structural evolution, and the optimization needs special procedures, e.g. incorporating topological derivatives [34], using a secondary level-set function [36], combining with other structural optimization techniques [37], etc. to generate new holes in the structural topology. The BESO method can generate discrete structures with well-defined structural boundaries [38,39], however, the method is greatly dependent on the heuristics employed in design-variable updating [40]. The design variable updating procedure is heavily reliant on the presence of a volume constraint, without which BESO method cannot be used. Moreover, the nonvolume constraints are incorporated in BESO using Lagrange multipliers, which leads to noisy convergence, especially when multiple nonvolume constraints are present in the problem [22]. The Sequential Element Reduction and Addition (SERA) technique uses improved heuristics [41] as compared to BESO but still retains the aforementioned disadvantages of BESO. The Canonical-Duality Theory (CDT) based structural optimization was first proposed by [42] and can produce discrete structures using duality principles of optimization [43] in polynomial-time, and was later also employed in [44,45]. Some improved versions of CDT are described thoroughly in [46,47]. The TOBS framework used herein yields discrete structures with well-defined boundaries like BESO, but is based on robust mathematical programming which enables the method to efficiently deal with multiple nonvolume constraints without the introduction of Lagrange multipliers [22,23]. Obtaining clear boundaries in the structural topologies at all iterations makes it straight-forward dealing with design-dependent pressure loads and finding material interfaces. The TOBS method is as simple as the element-based method SIMP, except that the design variables are strictly binary [22,48,49].

The TOBS method was introduced in [22] for single scale structural optimization demonstrating discrete structural topologies obtained through compliance minimization and volume minimization. An improved truncation error-regulating constraint was introduced into the TOBS method and clear 2D/3D microstructures were designed in [23] in the presence of several nonlinear constraints. The advantage of clear structural boundaries in dealing with design-dependent loads and thermomechanical problems was demonstrated in [50]. The generated ILPs in the TOBS method are solved using a commercial branch-and-bound solver in this work which is known to be of exponential computational complexity. One can also use polynomial-time methods to solve the generated ILPs, like CDT [18,43]. [49] applied the TOBS method to design optimal structural topologies considering fluid–structure interaction under laminar flow using a commercial Finite Element Analysis (FEA) package. A compact MATLAB code for optimizing structures using TOBS method considering multiple constraints is presented in an educational paper, TOBS-101 [51].

In this work, we aim at designing optimized structures with clear boundaries using binary design variables and integer programming, using the TOBS method. The suboptimization problems obtained by sequential linearization induce a truncation error. We introduce a novel constraint to maintain the truncation error low. The newly introduced constraint refrains the optimizer from making large changes in the structural topology by controlling the change in the total Young's moduli of elements. The TOBS method for single material structural optimization uses a similar constraint, which restrains the number of element flips (solid to void and vice-versa) each iteration [23]. We use the conventional mesh-independent sensitivity filtering to avoid checkerboarding and to achieve mesh-independence. Few examples of compliance minimization and mass minimization are shown to demonstrate discrete optimized structural topologies and smooth convergence obtained using TOBS. Discrete optimization-based multimaterial design using BESO can only work in the presence of volume constraints. All the examples shown in this work use a (nonlinear) mass/mean strain energy constraint and so they are the first discrete optimization-based multimaterial structures of their kind. Examples using design-dependent pressure loads and design-dependent self-weight loads are shown when two/three materials are made available for optimization. The opposing effects of the pressure loads and

self-weight loads are discussed through examples which converge at inactive constraint values. Material interface effects are neglected in this work, however introducing such effects is straightforward owing to the clearly defined material interfaces [31]. Through examples, it is also demonstrated that the TOBS method can smoothly converge at an inactive mass constraint value, depending on the action of different kinds of forces acting on the structure.

The manuscript is organized as follows. Section 2 describes multimaterial structural optimization and the pertinent interpolations of the properties of the materials. Section 3 discusses in detail, the TOBS method for single and multimaterial structural optimization, including: a novel truncation error-regulating constraint (Section 3.1), relaxation of constraints (Section 3.2) to generate feasible integer linear suboptimization problems each iteration, and the Integer Linear Programming solver based on the branch-and-bound method (Section 3.3). Section 4 shows the equilibrium equations with the stiffness matrix and force vectors for all the examples pertinent to the manuscript. Section 5 includes the adjoint sensitivity analysis of mean compliance for multimaterial structural optimization in the presence of design-dependent pressure and self-weight loads, and a mesh-independent sensitivity filtering (Section 5.1) used herein. Several examples for compliance minimization and mass minimization, including design-dependent loads are shown in Section 6, and examples which converge with an inactive constraint value are also demonstrated. Section 7 concludes the work and presents the key take-aways from this research.

2. Multimaterial structural topology optimization

We start by describing a structural topology optimization problem for single material,

$$\begin{aligned} \underset{m(x)\in\{m_s,\ m_v\}}{\text{Minimize}} \quad & f(m(\boldsymbol{x})) \\ \text{Subject to} \quad & g_i(m(\boldsymbol{x})) \leq \overline{g}_i \quad \forall\ i \in [1,\ N_g] \\ & \boldsymbol{x} \in \Omega_d \subset \mathbb{R}^{sd} \end{aligned} \tag{1}$$

where $\boldsymbol{x}$ signifies the spatial coordinate in the design domain Ω_d, which is a subset of the two-dimensional ($sd = 2$) space or three-dimensional ($sd = 3$) real space. $m(\cdot)$ denotes the material at any physical coordinate in Ω_d. For single material topology optimization, the possible materials $m(\cdot)$ at any $\boldsymbol{x} \in \Omega_d$ are solid material (m_s) and void material (m_v). $f(\cdot)$ is the objective function (see [42] for a discussion on the pertinent semantics) and $g_i(\cdot) \leq \overline{g}_i$ is the ith of the N_g inequality constraints in the optimization problem. The objective/constraint functions $f(\cdot)$ and $g_i(\cdot)$ can be some measures of structural performance, or measures of consumed resources.

The optimization problem in Eq. (1) is aimed at determining the choice of material at each and every physical coordinate of the design domain Ω_d which makes it an optimization problem with infinite design variables. The optimization problem can be made computationally tractable by approximating the design variables. One way to achieve this is by assuming the material choice to be uniform over finite cells/voxels/elements in the design domain. This method is used in methods like SIMP, BESO, and TOBS. Another way is to approximate the material choice is by using an implicit function, e.g. the level set method [32,33]. Using the element-based approximation in this work, the structural optimization problem can be simplified to

$$\begin{aligned} \underset{\boldsymbol{m}}{\text{Minimize}} \quad & f(\boldsymbol{m}) \\ \text{Subject to} \quad & g_i(\boldsymbol{m}) \leq \overline{g}_i \quad \forall\ i \in [1,\ N_g] \\ & m_j \in \{m_s,\ m_v\} \quad \forall\ j \in [1,\ N_e] \end{aligned} \tag{2}$$

where $\boldsymbol{m}$ is the vector of material choices, with each choice m_j uniform over an element in the design domain, and N_e is the number of elements in the design domain. This optimization problem is computationally tractable, and the problem is modeled using an interpolation between the solid m_s and void m_v material phases. A popular choice of interpolation is the modified SIMP interpolation,

$$E_j = (1 - \rho_j^p) \cdot E_{\min} + \rho_j^p \cdot E_s \tag{3}$$

where E_j signifies the material Young's modulus at element j via the design variable ρ_j, p is a penalty factor (usually 3, which realizes the Hazhin–Shtrikman bounds [52]), E_s is the Young's modulus of the solid material m_s, and $E_{\min}$ is a small number (e.g. $10^{-9} \cdot E_s$) to prevent singularities at analysis stage, and can be considered as the Young's modulus of the void material m_v. The design variable ρ_i indicates the presence of material (solid phase) when $\rho_j = 1$ and absence of material (void phase) when $\rho_j = 0$. The SIMP method used in [8,52] assumes

Table 1
Mapping between materials and design variables.

$\rho_{jk},\ k \in \{1,\ 2,\ 3,\ 4\}$	Material
0 0 0 0	Void
1 0 0 0	1
1 1 0 0	2
1 1 1 0	3
1 1 1 1	4

the design variables $\boldsymbol{\rho}$ to be continuous between 0 and 1, leading to optimal solutions with intermediate densities (i.e., $0 < \rho_j < 1$) which bear less physical meaning. Approaches like BESO and TOBS assume discrete variables $\boldsymbol{\rho}$ ensuring the design of manufacturable optimal structures. Using the interpolation in Eq. (3) and discrete design variables, the optimization problem in Eq. (2) becomes

$$\begin{aligned} \underset{\boldsymbol{\rho}}{\text{Minimize}} \quad & f(\boldsymbol{\rho}) \\ \text{Subject to} \quad & g_i(\boldsymbol{\rho}) \leq \overline{g}_i \quad \forall\ i \in [1,\ N_g] \\ & \rho_j \in \{0,\ 1\} \quad \forall\ j \in [1,\ N_e] \end{aligned} \tag{4}$$

Extending Eq. (2), a multimaterial structural topology optimization can be defined as

$$\begin{aligned} \underset{\boldsymbol{m}}{\text{Minimize}} \quad & f(\boldsymbol{m}) \\ \text{Subject to} \quad & g_i(\boldsymbol{m}) \leq \overline{g}_i \quad \forall\ i \in [1,\ N_g] \\ & m_j \in \{m_1,\ m_2, \ldots,\ m_{N_m}\} \quad \forall\ j \in [1,\ N_e] \end{aligned} \tag{5}$$

where N_m is the number of materials available for optimization. Similar to the single material problem, we again need an interpolation to model the structural properties. In this work, the different materials used for structural optimization differ only in Young's modulus. We use the extended SIMP formulation, which is a generalized form of Eq. (3),

$$E_j = \sum_{k=1}^{N_m} \left(1 - \rho_{jk}^p\right) \left[\prod_{t=1}^{k-1} \rho_{jt}^p\right] E_{s_{k-1}} + \prod_{t=1}^{N_m} \rho_{jt}^p E_{s_{N_m}} \tag{6}$$

where E_j is the Young's modulus of element j, E_{s_k} is the Young's modulus of solid material m_k, $E_{s_0} = E_{\min}$ is a small number to avoid singularity at analysis stage, ρ_{jk} is the kth design variable corresponding to element j, and p is a penalization factor (3 in this work). In this work, we use

$$E_{min} = 10^{-9} \cdot \texttt{min}\left(E_{s_1},\ E_{s_2}, \ldots,\ E_{s_{N_m}}\right) \tag{7}$$

We can observe that the modified SIMP interpolation in Eq. (3) can be obtained by substituting $N_m = 1$ in the extended SIMP interpolation in Eq. (3). For two materials ($N_m = 2$) and three materials ($N_m = 3$) in structural optimization, the extended SIMP interpolation is respectively,

$$\begin{aligned} E_j &= \left(1 - \rho_{j1}^p\right) E_{\min} + \rho_{j1}^p \left[\left(1 - \rho_{j2}^p\right) E_1 + \rho_{j2}^p E_2\right] \\ E_j &= \left(1 - \rho_{j1}^p\right) E_{\min} + \rho_{j1}^p \left[\left(1 - \rho_{j2}^p\right) E_1 + \rho_{j2}^p \left(\left(1 - \rho_{j3}^p\right) E_2 + \rho_{j3}^p E_3\right)\right] \end{aligned} \tag{8}$$

From Eq. (8), we can observe that the first design variable ρ_{j1} decides the presence of any material: $\rho_{j1} = 0$ for void phase at element j, and $\rho_{j1} = 1$ for one of the N_m solid materials at element j. If $\rho_{j1} = 1$, the second design variable ρ_{j2} implies material m_1 at element j if $\rho_{j2} = 0$, and implies some other material $m_k,\ k > 1$ if $\rho_{j2} = 1,\ \rho_{j3} = 0$. Similarly, if $\rho_{j1} = \rho_{j2} = 1$, the third design variable ρ_{j3} indicates material m_2 if $\rho_{j3} = 0$, and material m_3 if $\rho_{j3} = 1$. To summarize, the design variables and the materials implied at any element j for $N_m = 4$ are presented in Table 1. It should be noted that the mapping shown in Table 1 is nonunique in that, nonunique permutations of 0/1 design variables map to the same material. For e.g. both 0 0 0 0 and 0 1 0 0 map to the void material phase by the extended SIMP interpolation. We use a simple strategy during structural optimization to

avoid potential issues due to this behavior of the extended SIMP formulation, which will be discussed in the next section.

The mass density is also interpolated in a similar way as that of the Young's modulus, but with unit penalty,

$$\begin{aligned}\gamma_j &= \rho_{j1}\left[\left(1-\rho_{j2}\right)\gamma_1 + \rho_{j2}\gamma_2\right] \\ \gamma_j &= \rho_{j1}\left[\left(1-\rho_{j2}\right)\gamma_1 + \rho_{j2}\left(\left(1-\rho_{j3}\right)\gamma_2 + \rho_{j3}\gamma_3\right)\right]\end{aligned} \tag{9}$$

We should note that the mass density of the void material is 0. Herein, we use the penalty values $p = 3$ and $p = 1$ for Young's modulus and mass density respectively. The mass of the structure at any iteration of optimization can be simply computed using

$$w(\boldsymbol{\rho}) = \sum_{j=1}^{N_e} \gamma_j V_j \tag{10}$$

where V_j is the volume (area in 2D) of the element j.

The use of continuous variables for multimaterial structural optimization leads to unclear boundaries (due to intermediate densities) in the optimal solution, just like the single material structural optimization. Moreover, the nonbinary values of design variables lead to some elements having a mixture of available materials, which not only bears less physical meaning, but also makes the material interface uncertain. If one were to consider and model material interface effects during analysis, a clear interface between participating materials in optimization is required. Although this work does not incorporate material interfacing effects, the clear material interfaces guaranteed during optimization help in incorporating such effects with ease. The unclear boundaries also make the determination of design dependent surface loads, e.g. hydrostatic pressure loads nontrivial. This work employs binary values for the design variables, i.e., $\rho_{jk} \in \{0,\ 1\}$ enabling clear boundaries.

Using the extended SIMP interpolation and discrete design variables, the multimaterial structural topology optimization can be modeled as

$$\begin{aligned}&\underset{\boldsymbol{\rho}}{\text{Minimize}} \quad f(\boldsymbol{\rho}) \\ &\text{Subject to} \quad g_i(\boldsymbol{\rho}) \le \overline{g}_i \quad \forall\ i \in [1,\ N_g] \\ &\qquad\qquad \rho_{jk} \in \{0,\ 1\} \quad \forall\ j \in [1,\ N_e],\ k \in [1,\ N_m]\end{aligned} \tag{11}$$

where $\boldsymbol{\rho}$ is the matrix of design variables of size $N_e \times N_m$. This optimization problem is solved via linearization and integer programming in this work, as described in the latter sections.

3. Topology optimization of binary structures considering multiple materials

The optimization problem in Eq. (11) involves objective $f(\cdot)$ and constraint $g(\cdot)$ functions. This optimization is in general nonconvex. One way to solve such nonlinear optimization problems is via sequential approximation in which, a sequence of suboptimization problems is generated based on the derivative information of the objective/constraint functions and is solved using efficient optimization methods available in literature. In this work, we use Linear approximation of the objective/constraint functions to generate the suboptimization problems. Since we consider binary design variables for the parent optimization problem in Eq. (11), the design variables of the linear suboptimization problems are integers. The optimization of such linear problems with integer constraints is called Integer Linear Programming (ILP).

The ILP problem is generated using the first derivative information of the objective/constraint functions. These derivatives are computed with respect to the design variables of the parent optimization problem in Eq. (11) and are called sensitivities. The derivation of sensitivities for the objective/constraint functions used in this manuscript is discussed in the next section. The ILP problem is an approximation of the parent optimization problem (Eq. (11)) about the current state of design variables. Consider the Taylor's series approximation of the objective/constraint functions,

$$\begin{aligned}f(\boldsymbol{\rho}) &= f(\boldsymbol{\rho}^n) + \frac{\partial f}{\partial \boldsymbol{\rho}}(\boldsymbol{\rho}^n) : \Delta\boldsymbol{\rho}^n + HOT \\ g(\boldsymbol{\rho}) &= g(\boldsymbol{\rho}^n) + \frac{\partial g}{\partial \boldsymbol{\rho}}(\boldsymbol{\rho}^n) : \Delta\boldsymbol{\rho}^n + HOT\end{aligned} \tag{12}$$

where $\boldsymbol{\rho}^n$ is the matrix of design variables at current state n of the parent optimization problem (Eq. (11)), $\frac{\partial f}{\partial \boldsymbol{\rho}}(\boldsymbol{\rho}^n)$ and $\frac{\partial g}{\partial \boldsymbol{\rho}}(\boldsymbol{\rho}^n)$ are the matrices of first derivatives (sensitivities) computed using the current state, $\Delta\boldsymbol{\rho}^n$ is the matrix of design variable updates, and HOT are the higher order terms. ILP problem is generated using linear approximation, i.e., by neglecting the higher order terms in Eq. (12). Using the linear approximation of the Taylor's expansion, the generated suboptimization problem can be written as

$$\begin{aligned} &\underset{\Delta\boldsymbol{\rho}^n}{\text{Minimize}} \quad \frac{\partial f}{\partial \boldsymbol{\rho}}(\boldsymbol{\rho}^n) : \Delta\boldsymbol{\rho}^n \\ &\text{Subject to} \quad \frac{\partial g_i}{\partial \boldsymbol{\rho}}(\boldsymbol{\rho}^n) : \Delta\boldsymbol{\rho}^n \leq \overline{g}_i - g_i(\boldsymbol{\rho}^n) \quad \forall\ i \in [1,\ N_g] \\ &\qquad \Delta\rho^n_{jk} \in \{-\rho^n_{jk},\ 1-\rho^n_{jk}\} \quad \forall\ j \in [1,\ N_e],\ k \in [1,\ N_m] \end{aligned} \tag{13}$$

where $\Delta\rho^n_{jk}$ is the update of the kth design variable corresponding to the jth element, at nth iteration (state). Optimizing the ILP problem, the design variables are simply updated using

$$\boldsymbol{\rho}^{n+1} = \boldsymbol{\rho}^n + \Delta\boldsymbol{\rho}^n \tag{14}$$

The linearized problem in Eq. (13) is sufficiently accurate only for a small number of changes in the element phases. This is because the linear approximation of the objective/constraint functions neglects the higher order terms HOT in their Taylor's expansions (Eq. (12)). This difference is called the truncation error and can be estimated as $\mathcal{O}\left(\|\Delta\boldsymbol{\rho}\|^2\right)$. In order to maintain the ILP problem in Eq. (13) well-approximating the parent optimization problem (Eq. (11)) in a neighborhood of the current state n, we constrain the possible change in the design variables each iteration. Such a constraint is aimed at keeping the truncation error of the Taylor's expansions of the objective/constraint functions small.

3.1. Truncation error-regulating constraint

In this work, the different materials considered for multimaterial structural optimization are assumed to be isotropic, with same Poisson's ratios but different Young's moduli. The N_m design variables corresponding to each element are interpolated using extended SIMP (Eq. (6)) to obtain the material choice, or in this case, the Young's modulus of the element. The objective/constraint functions directly depend on the Young's moduli of the elements which in turn depend on the design variables. The dependency of objective/constraint functions on the Young's moduli is discussed clearly in the later sections. The Taylor's expansion of the objective/constraint functions can be written in terms of Young's modulus as

$$\begin{aligned} f(\boldsymbol{E}(\boldsymbol{\rho})) &= f(\boldsymbol{E}(\boldsymbol{\rho}^n)) + \frac{\partial f}{\partial \boldsymbol{E}}(\boldsymbol{\rho}^n) \cdot \Delta\boldsymbol{E} + \mathcal{O}\left(\|\Delta\boldsymbol{E}\|^2\right) \\ g(\boldsymbol{E}(\boldsymbol{\rho})) &= g(\boldsymbol{E}(\boldsymbol{\rho}^n)) + \frac{\partial g}{\partial \boldsymbol{E}}(\boldsymbol{\rho}^n) \cdot \Delta\boldsymbol{E} + \mathcal{O}\left(\|\Delta\boldsymbol{E}\|^2\right) \end{aligned} \tag{15}$$

where $\boldsymbol{E}$ is the vector of Young's moduli of the elements. To control the truncation error in Eq. (15), it is reasonable to constrain the change in Young's moduli, $\Delta\boldsymbol{E}$. We impose a novel constraint on the design variables $\Delta\boldsymbol{\rho}$ of the ILP problem by restraining $\Delta\boldsymbol{E}$. We propose a one-norm constraint on the change in Young's moduli vector $\Delta\boldsymbol{E}$,

$$\|\Delta\boldsymbol{E}\|_1 \leq \beta \cdot N_e E_{s_{N_m}} \tag{16}$$

where $\|\Delta\boldsymbol{E}\|_1 = \sum_{j=1}^{N_e} \Delta E_j$ is the one norm of the vector $\Delta\boldsymbol{E}$, β is a small number (say 0.05) to regulate the truncation error $\mathcal{O}\left(\|\Delta\boldsymbol{E}\|^2\right)$. The right hand side of the inequality constraint in Eq. (16) is β multiplied by the sum of Young's moduli of all N_e elements in the design domain Ω_d when the elements are filled by the stiffest material m_{N_m} (with Young's modulus $E_{s_{N_m}}$). The change in Young's modulus of any element ΔE_j can be written in terms of change in design variables using chain rule,

$$\Delta E_j = \sum_{k=1}^{N_m} \frac{\partial E_j}{\partial \rho^n_{jk}} \cdot \Delta\rho^n_{jk} \tag{17}$$

Using the chain rule in Eq. (16), we arrive at an inequality constraint in terms of the design variables $\Delta\boldsymbol{\rho}$ of the suboptimization (ILP) problem,

$$\|\Delta \boldsymbol{E}\|_1 = \sum_{j=1}^{N_e} \left| \frac{\partial E_j}{\partial \boldsymbol{\rho}^n} : \Delta \boldsymbol{\rho}^n \right| \leq \beta \cdot N_e E_{s_{N_m}} \tag{18}$$

The constraint in Eq. (18) is nonlinear, and we need a linear constraint to be incorporated in the ILP problem (Eq. (13)). Consider the inequality,

$$\left| \sum_{k=1}^{N_m} \frac{\partial E_j}{\partial \rho_{jk}^n} \cdot \Delta \rho_{jk}^n \right| \leq \sum_{k=1}^{N_m} \left| \frac{\partial E_j}{\partial \rho_{jk}^n} \cdot \Delta \rho_{jk}^n \right| \tag{19}$$

This inequality implies that the set of design variables $\Delta\boldsymbol{\rho}$ of the ILP problem which satisfies

$$\sum_{j=1}^{N_e} \sum_{k=1}^{N_m} \left| \frac{\partial E_j}{\partial \rho_{jk}^n} \cdot \Delta \rho_{jk}^n \right| \leq \beta \cdot N_e E_{s_{N_m}} \tag{20}$$

also satisfies the truncation error-regulating constraint in Eq. (18), with Eq. (20) being conservative. The left hand side of the inequality constraint (Eq. (20)) appears nonlinear, but is in fact linear when binary design variables are used (as in this work). Each term in the double summation in Eq. (20) can be written as

$$\left| \frac{\partial E_j}{\partial \rho_{jk}^n} \cdot \Delta \rho_{jk}^n \right| = \left| \frac{\partial E_j}{\partial \rho_{jk}^n} \right| \cdot \left| \Delta \rho_{jk}^n \right| = \left| \frac{\partial E_j}{\partial \rho_{jk}^n} \right| \cdot \alpha_{jk}^n \Delta \rho_{jk}^n \tag{21}$$

where $\left| \frac{\partial E_j}{\partial \rho_{jk}^n} \right|$ can be computed using the extended SIMP interpolation (Eq. (6)) and will also be discussed in the later sections, and α_{jk}^n is given by

$$\alpha_{jk}^n = \begin{cases} 1 & : \rho_{jk}^n = 0 \\ -1 & : \rho_{jk}^n = 1 \end{cases} \tag{22}$$

Using Eq. (22), the truncation error-regulating constraint is written in linear form and can be incorporated in the ILP problem. The specific values of α_{jk}^n given in Eq. (22) are available only because of the binary nature of design variables. We do not know at state n the design variables in the next state (ρ_{jk}^{n+1}) so as to determine $\Delta\rho_{jk}^n$ (observe Eq. (14)). The absolute value of the change in design variables if $\rho_{jk}^n = 0$ is given by

$$\left| \Delta \rho_{jk}^n \right| = \begin{cases} 0 = \alpha_{jk}^n \Delta \rho_{jk}^n & : \rho_{jk}^{n+1} = 0 \\ 1 = \alpha_{jk}^n \Delta \rho_{jk}^n & : \rho_{jk}^{n+1} = 1 \end{cases} \tag{23}$$

and if $\rho_{jk} = 1$ is given by

$$\left| \Delta \rho_{jk}^n \right| = \begin{cases} 1 = \alpha_{jk}^n \Delta \rho_{jk}^n & : \rho_{jk}^{n+1} = 0 \\ 0 = \alpha_{jk}^n \Delta \rho_{jk}^n & : \rho_{jk}^{n+1} = 1 \end{cases} \tag{24}$$

From the Eqs. (23) ad (24), we see that using the α_{jk}^n as defined in Eq. (22), we can correctly define the absolute value of $\Delta\rho_{jk}^n$. The ILP problem along with the truncation error-regulating constraint can be thus written as

$$\begin{aligned} \underset{\Delta \boldsymbol{\rho}^n}{\text{Minimize}} \quad & \frac{\partial f}{\partial \boldsymbol{\rho}}(\boldsymbol{\rho}^n) : \Delta \boldsymbol{\rho}^n \\ \text{Subject to} \quad & \frac{\partial g_i}{\partial \boldsymbol{\rho}}(\boldsymbol{\rho}^n) : \Delta \boldsymbol{\rho}^n \leq \overline{g}_i - g_i(\boldsymbol{\rho}^n) \quad \forall\ i \in [1,\ N_g] \\ & \sum_{j=1}^{N_e} \sum_{k=1}^{N_m} \left| \frac{\partial E_j}{\partial \rho_{jk}^n} \right| \alpha_{jk}^n \cdot \Delta \rho_{jk}^n \leq \beta \cdot N_e E_{s_{N_m}} \\ & \Delta \rho_{jk}^n \in \{-\rho_{jk}^n,\ 1 - \rho_{jk}^n\} \quad \forall\ j \in [1,\ N_e],\ k \in [1,\ N_m] \end{aligned} \tag{25}$$

The truncation error-regulating constraint derived here for multimaterial optimization problems can be observed as a generalization of the truncation error-regulating constraint defined for single material optimization problems in

our earlier works [23,50]. In multimaterial optimization, when design variables are updated, they affect the quantities in elasticity (like the mean compliance) via the Young's modulus. The linearization in terms of the Young's modulus as shown in Eq. (15) is crucial, and controlling the truncation error in terms of change in the Young's modulus is more accurate. The use of change in Young's moduli to restrain the truncation error also imparts some stability to the optimization, especially for problems involving materials with very different Young's moduli. The truncation error-regulating constraint in [23], when applied to multimaterial problems, treats the switching between any two available materials as the same, without regard to the underlying material properties. The new truncation error-regulating constraint proposed here factors in the difference in the Young's moduli of the materials, and so a larger truncation error is assigned to elements where material can switch from a very stiff material to a very flexible material, and a smaller truncation error is assigned to elements where material can switch between two materials with smaller difference in their Young's moduli. This imparts additional stability to the algorithm preventing rapid switching (if any) between materials with very different properties. The examples shown in this work show stably converged optimized solutions even when the considered materials are very different in their Young's moduli, showing that the derived constraint restrains from rapid change in structural topology each iteration, is mathematically accurate and helps in a stable convergence.

This work uses linearization with respect to the Young's modulus given that the problems considered in this work consider elastic analyses. For other physics, different material properties can be adopted for the linearization and truncation error-control, e.g. thermal conductivity for heat conduction problems, etc.

3.2. Relaxation of constraints

The truncation error-regulating constraint in Eq. (25) allows only small changes in the structural topology each iteration. Assuming the constraints $g_i(\boldsymbol{\rho})$ are sufficiently smooth, small changes in the structural topology permit only small changes in the value of constraints each iteration. This can make the ILP suboptimization problem in Eq. (25) infeasible when there is no set of possible design variables $\Delta\boldsymbol{\rho}^n$ which can satisfy any of the N_g linearized constraints. This situation is commonly observed when the right hand side $\overline{g}_i$ of any constraint is far from being feasible ($\overline{g}_i > g_i(\boldsymbol{\rho}^n)$) in the current state of design variables. For example, consider the single material topology optimization with a volume constraint of 50%, with the structural topology having 100% volume at the current state.

In order to avoid this infeasibility of the ILP subproblems, we relax the constraints each iteration so that we generate feasible ILP subproblems at each iteration n. We use the constraint relaxation [50],

$$\Delta g_i^n = \begin{cases} -\epsilon_i g_i(\boldsymbol{\rho}^n) & : \overline{g}_i < (1-\epsilon_i) g_i(\boldsymbol{\rho}^n) \\ \overline{g}_i - g_i(\boldsymbol{\rho}^n) & : \overline{g}_i \in \left[(1-\epsilon_i) g_i(\boldsymbol{\rho}^n),\ (1+\epsilon_i) g_i(\boldsymbol{\rho}^n)\right] \\ \epsilon_i g_i(\boldsymbol{\rho}^n) & : \overline{g}_i > (1+\epsilon_i) g_i(\boldsymbol{\rho}^n) \end{cases} \tag{26}$$

where Δg_i^n is the relaxed right hand side of the ith linear inequality constraint in the ILP problem (Eq. (25)), and ϵ_i is the relaxation parameter. Effectively, Eq. (26) restrains the bounds (right hand sides) of each constraint i to be within a factor ϵ_i of the current constraint value ($g_i(\boldsymbol{\rho}^n)$).

The ILP subproblem incorporating truncation error-regulating constraint and constraints' relaxation is given by

$$\begin{aligned} \underset{\Delta\boldsymbol{\rho}^n}{\text{Minimize}} \quad & \frac{\partial f}{\partial \boldsymbol{\rho}}(\boldsymbol{\rho}^n) : \Delta\boldsymbol{\rho}^n \\ \text{Subject to} \quad & \frac{\partial g_i}{\partial \boldsymbol{\rho}}(\boldsymbol{\rho}^n) : \Delta\boldsymbol{\rho}^n \leq \Delta g_i^n \quad \forall\ i \in [1,\ N_g] \\ & \sum_{j=1}^{N_e} \sum_{k=1}^{N_m} \left| \frac{\partial E_j}{\partial \rho_{jk}^n} \right| \alpha_{jk}^n \cdot \Delta\rho_{jk}^n \leq \beta \cdot N_e E_{s_{N_m}} \\ & \Delta\rho_{jk}^n \in \{-\rho_{jk}^n,\ 1-\rho_{jk}^n\} \quad \forall\ j \in [1,\ N_e],\ k \in [1,\ N_m] \end{aligned} \tag{27}$$

where Δg_i^n is computed using Eq. (26). This is the final form of ILP subproblem generated each iteration in the TOBS framework for multimaterials, and is solved using an Integer Programming solver. The design variables $\boldsymbol{\rho}^n$ are then updated using Eq. (14), and the procedure is continued until a specified convergence criterion is met.

3.3. Integer linear programming (ILP) solver

As explained earlier, ILP problem is an LP problem with added integer constraints on design variables. This can lead to slightly suboptimal solutions yielded by optimizing ILP problem as compared to optimizing the LP problem. However, the structural topology obtained by solving ILP problems has clear boundaries/material interfaces and is manufacturable.

In this work, we use the branch-and-bound algorithm implemented in the CPLEX package to solve the ILP problem generated each iteration. The branch-and-bound method works by first solving the LP version of the ILP problem, i.e., the ILP problem without any integer constraints using some LP solver, e.g. simplex method. Based on the optimal solution of this problem, the optimization problem is branched into more LP problems with added integer constraints on some design variables. These LP problems are solved with the new integer constraints, and then branched again until a perfectly integer solution is obtained. Fig. 1 shows a schematic for a hypothetical integer program with two design variables $\{x,\ y\}$. The integer program is first solved without the integer constraints using an existing optimization method. Branching is then made adding extra inequality constraints with integer bounds on some design variables (in the schematic, x first then y) to generate newer optimization problems. The new optimization problems are solved using some conventional optimization technique again. This process of branching and bounding is continued until an optimal integer solution is encountered or when all the leaf nodes of the branch-and-bound tree yield infeasible solutions. When multiple integer solutions are available at the tree leaves, the solution with the best objective function is used as the optimal solution. We use the `cplexmilp` function of the CPLEX package in MATLAB in this work for solving the ILP problems. One can also use `intlinprog` functionality of MATLAB to solve the ILP problem as discussed in [22,51].

The branch-and-bound method used in this work is NP-hard, and so the computational cost of solving the ILP problem is in general higher than that of the LP problem, since the branch-and-bound solver involves solving many LP problems. However, the bottleneck of structural optimization is Finite Element Analysis and the computational cost of integer programming is less significant for finer meshes as demonstrated in [50]. [50] demonstrates that the branch-and-bound solver from CPLEX takes much less computational time during topology optimization as compared to 2D FEA problems, and so is computationally tractable. This effect is more pronounced in 3D FEA problems due to solving matrix systems with larger bandwidth and problems involving nonlinear analyses.

A convergence criterion is used to stop iterating over the topologies. In this work, the convergence criterion used at any iteration c is given by

$$\begin{aligned} &2.\frac{\max\limits_{j\in[c-4,\ c]}\{f_j\}-\min\limits_{j\in[c-4,\ c]}\{f_j\}}{\max\limits_{j\in[c-4,\ c]}\{f_j\}+\min\limits_{j\in[c-4,\ c]}\{f_j\}}\leq\tau \\ &g_i\leq\bar{g}_i\ \forall i\in[1,\ N_g] \\ &c\leq 300 \end{aligned} \tag{28}$$

where τ is a user-defined tolerance. In short, the optimization is stopped when the objective function value does not change much over the last 5 iterations whilst all the constraints are satisfied, or the number of iterations reaches 300.

In summary, the TOBS method involves the following stages: 1. The parent optimization problem is sequentially approximated (linearly in this work), a truncation error-regulating constraint is added, and the constraints are relaxed to generate the integer suboptimization problems. 2. The equilibrium equations governing the physics of the problem (discussed in the next section) are solved to obtain the state variables. 3. The coefficients of the suboptimization problems are the derivatives of quantities which can depend on the state variables computed. These derivatives (called sensitivities) are computed using methods like adjoint sensitivity analysis, discussed in the next sections. 4. The suboptimization problems are solved using the sensitivities, and the design variables $\boldsymbol{\rho}$ are updated. 5. This cycle is repeated until a chosen convergence criterion (Eq. (28)) is satisfied.

4. Finite element analysis

In this section, we discuss the equilibrium equations involved in determining the state variables of the problem at hand. In this work, we solve optimization problems related to linear static structural analysis with and without design-dependent surface and design-dependent volumetric loads, for two-dimensional design domains.

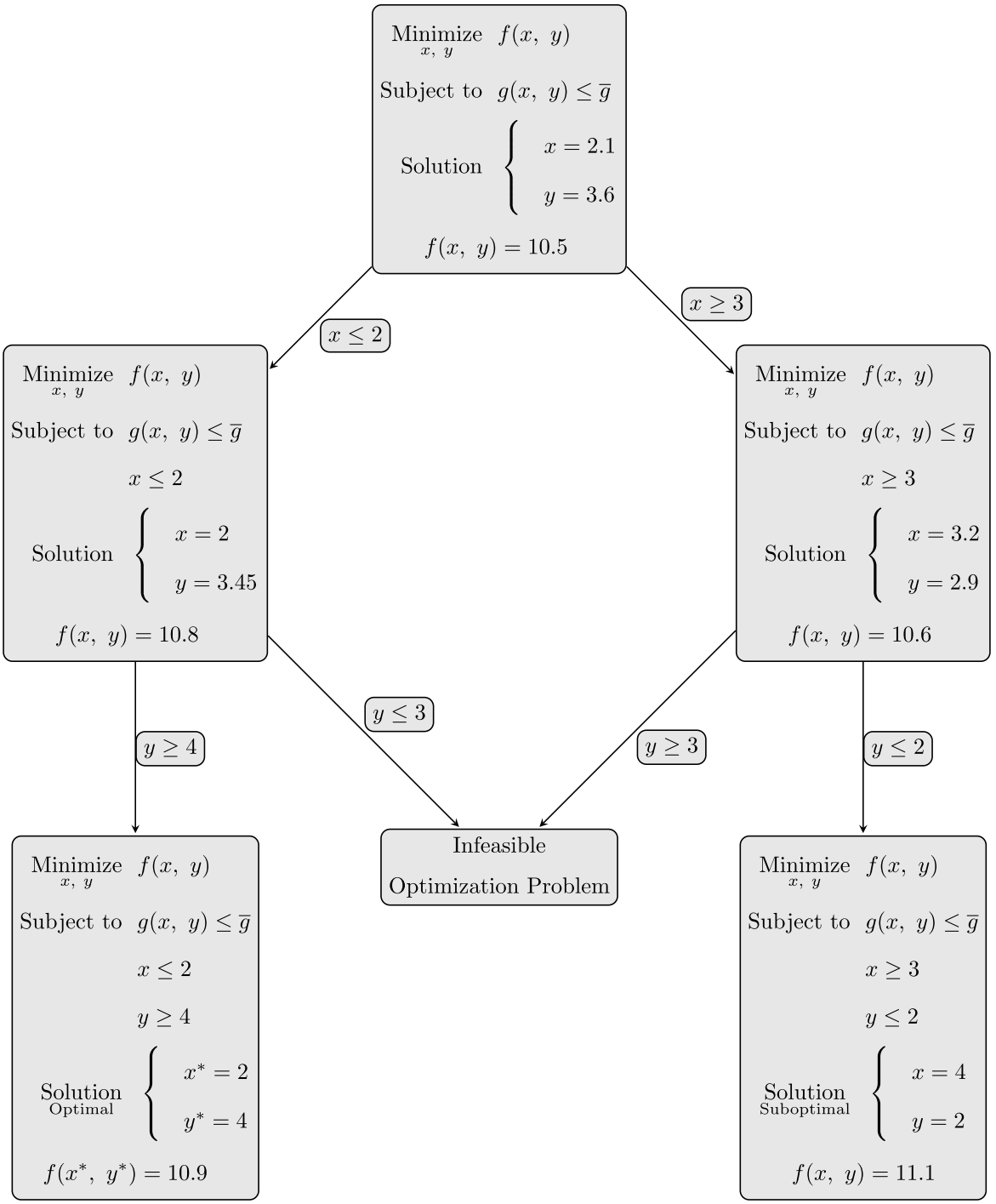

Fig. 1. Schematic of branch-and-bound method for an integer program.

Given the design domain Ω_d, the equilibrium equations for linear elastostatics are given in Table 2, where $\boldsymbol{\sigma}$ is the vector of stresses, $\boldsymbol{\epsilon}$ is the strain vector, $\boldsymbol{b}$ is the volumetric loads, $\boldsymbol{D}$ is the elasticity tensor in Voigt form, $\boldsymbol{u}$ is the vector of displacements, $\boldsymbol{g}$ is the specified displacements on boundary Γ_g and $\boldsymbol{t}$ is the vector of surface tractions specified on a subset Γ_t of the boundary Γ.

Table 2
Strong form of Linear Elastostatics.

$\nabla \cdot \boldsymbol{\sigma} + \boldsymbol{b} = \boldsymbol{0}$	Equilibrium equation
$\boldsymbol{\sigma} = \boldsymbol{D} \cdot \boldsymbol{\epsilon}$	Constitutive equation
$\boldsymbol{\epsilon} = \frac{1}{2} \cdot (\nabla \boldsymbol{u} + \nabla \boldsymbol{u}^T)$	Kinematic compatibility
$\boldsymbol{u} = \boldsymbol{g}, \ \boldsymbol{x} \in \Gamma_g \subset \Gamma$	Essential Boundary Conditions
$\boldsymbol{\sigma} \cdot \boldsymbol{n} = \boldsymbol{t}, \ \boldsymbol{x} \in \Gamma_t \subset \Gamma$	Natural Boundary Conditions
$\boldsymbol{u} : \ \Omega_d \rightarrow \mathbb{R}^{sd}$	Solution Map

The variational form of the linear elastostatics problem in Table 2 is given by

$$\int_{\Omega_d} \delta \boldsymbol{\epsilon}^T \boldsymbol{D} \boldsymbol{\epsilon} \ d\Omega = \int_{\Omega_d} \delta \boldsymbol{u}^T \boldsymbol{b} \ d\Omega + \int_{\Gamma_t} \delta \boldsymbol{u}^T \boldsymbol{t} \ d\Gamma \tag{29}$$

where $\delta(\cdot)$ signifies the variation of a quantity. We use the finite element interpolations,

$$\begin{aligned} \boldsymbol{u} &= \boldsymbol{N} \boldsymbol{u}^h \quad \delta \boldsymbol{u} = \boldsymbol{N} \delta \boldsymbol{u}^h \\ \boldsymbol{\epsilon} &= \boldsymbol{B} \boldsymbol{u}^h \quad \delta \boldsymbol{\epsilon} = \boldsymbol{B} \delta \boldsymbol{u}^h \end{aligned} \tag{30}$$

where $\boldsymbol{N}$ is the matrix of shape function values, $\boldsymbol{B}$ is the matrix of shape function gradients and $\boldsymbol{u}^h$ are the nodal displacements. We drop the $(\cdot)^h$ superscript herein for the sake of brevity. Incorporating the finite element interpolations into the weak form in Eq. (29) converts it into a matrix form,

$$\boldsymbol{K} \boldsymbol{u} = \boldsymbol{F} \tag{31}$$

where the matrices in the matrix form are given by

$$\begin{aligned} \boldsymbol{K} &= \sum_{e=1}^{N_e} \int_{\Omega_e} \boldsymbol{B}_e^T \boldsymbol{D}_e \boldsymbol{B}_e \ d\Omega = \sum_{e=1}^{N_e} \boldsymbol{K}_e \\ \boldsymbol{F} &= \sum_{e=1}^{N_e} \left(\int_{\Omega_e} \boldsymbol{N}_e^T \boldsymbol{b}_e \ d\Omega + \sum_{b \in \Gamma_t \cap \Gamma_e} \int_{\Gamma_b} \boldsymbol{G}_b^T \boldsymbol{t}_b \ d\Gamma \right) = \sum_{e=1}^{N_e} \boldsymbol{F}_e \end{aligned} \tag{32}$$

where Ω_e is the domain of finite element e, $\boldsymbol{D}_e$, $\boldsymbol{b}_e$, $\boldsymbol{N}_e$ and $\boldsymbol{B}_e$ are respectively the elasticity tensor, body force vector, shape function matrix, and shape function gradient matrix of finite element e. $\boldsymbol{K}_e$ and $\boldsymbol{F}_e$ are respectively the elemental stiffness matrix and elemental force vector. $\boldsymbol{G}_b$ is the shape functions matrix of the boundary edge/surface finite element b and $\boldsymbol{t}_b$ is the corresponding traction vector. In this work, the only traction loads considered are the hydrostatic pressure loads, i.e.,

$$\boldsymbol{p}_b = -t \boldsymbol{n}_b \tag{33}$$

where t is the constant pressure and $\boldsymbol{n}_b$ is the outward normal vector to the boundary edge/surface element b. In the examples shown where pressure loads are considered, we use unit hydrostatic pressure load $t = 1.0$. Since the elasticity matrix $\boldsymbol{D}_e$ has the Young's modulus as a factor, the interpolation in Eq. (8) is also applicable to the elasticity matrix. The pressure loads are applied as part of the second term of the force vector in Eq. (32). The force vector corresponding to just the hydrostatic pressure loads is given by

$$\sum_{e=1}^{N_e} \rho_{e1} \sum_{b \in \Gamma_{fs} \cap \Gamma_e} \int_{\Gamma_b} \boldsymbol{G}_b^T \boldsymbol{p}_b \ d\Gamma \tag{34}$$

where Γ_{fs} is the fluid–structure boundary. The pressure loads on an element e are nonzero only if the element is solid (i.e., $\rho_{e1} = 1$). In this work, we assign the fluid elements each iteration using the concept of fluid flooding [53]. We start with regions in the design domain where the fluid is already present. Using a Breadth-First Search (BFS) approach, for each fluid element, we assign the neighboring void elements as fluid and add the newly fluid-assigned elements to the queue used in the BFS algorithm.

The self-weight loads acting at every point in the domain are proportional to the mass density. The force vector corresponding to the self-weight loads is given by

$$\sum_{e=1}^{N_e} \int_{\Omega_e} \gamma_e \boldsymbol{N}_e^T \boldsymbol{g} \; d\Omega \tag{35}$$

where γ_e is the mass density of the material in element e, and $\boldsymbol{g}$ is the vector signifying acceleration due to gravity.

5. Sensitivity analysis

Gradient-based optimization methods like the TOBS method use the gradients of objective/constraint functions to iterate over the solutions. These gradients are called sensitivities and are used in the optimization problem in Eq. (27). In this work, we use the mean strain energy (often referred to as mean compliance in the field of structural optimization) and mass functions for optimization. We also consider design-dependent pressure loads and design-dependent self-weight loads for this purpose.

The mean compliance (or the mean strain energy) of a structure at any iteration is given by

$$C(\boldsymbol{\rho},\ \boldsymbol{E},\ \boldsymbol{\gamma}) = \frac{1}{2}\boldsymbol{u}^T \boldsymbol{K}\boldsymbol{u} = \sum_{e=1}^{N_e} \frac{1}{2}\boldsymbol{u}_e^T \boldsymbol{K}_e \boldsymbol{u}_e \tag{36}$$

where $\boldsymbol{u}_e$ is the vector of elemental displacements, $\boldsymbol{\rho}$ is the matrix of design variables, $\boldsymbol{E}$ and $\boldsymbol{\gamma}$ are the vectors of elemental Young's moduli and mass densities at any iteration. The adjoint sensitivity analysis is used to compute the sensitivities of mean compliance. The adjoint form of the mean compliance function is written using the state equilibrium equation in Eq. (31) as

$$C(\boldsymbol{\rho},\ \boldsymbol{E},\ \boldsymbol{\gamma}) = \frac{1}{2}\boldsymbol{u}^T \boldsymbol{K}\boldsymbol{u} + \boldsymbol{\lambda}^T(\boldsymbol{K}\boldsymbol{u} - \boldsymbol{F}) \tag{37}$$

where $\boldsymbol{\lambda}$ is the adjoint variable vector. Since this manuscript employs linear elastostatics as the analysis procedure, mean compliance is dependent on the design variables through Young's modulus and mass density (in case of self-weight loads). The sensitivities of the mean compliance can be computed using the chain rule,

$$\frac{\partial C}{\partial \rho_{jk}}(\boldsymbol{\rho},\ \boldsymbol{E},\ \boldsymbol{\gamma}) = \frac{\partial C(\boldsymbol{\rho})}{\partial \rho_{jk}} + \frac{\partial C(\boldsymbol{E})}{\partial E_j} \cdot \frac{\partial E_j}{\partial \rho_{jk}} + + \frac{\partial C(\boldsymbol{\gamma})}{\partial \gamma_j} \cdot \frac{\partial \gamma_j}{\partial \rho_{jk}} \tag{38}$$

where E_j is the Young's modulus and γ_j is the mass density of element j. The design variable affects the mean compliance only through the Young's modulus when design-dependent pressure loads and self-weight loads are absent. The gradients of mean compliance with respect to the Young's modulus are then given by

$$\frac{\partial C(\boldsymbol{E})}{\partial E_j} = \boldsymbol{u}^T \boldsymbol{K} \frac{\partial \boldsymbol{u}}{\partial E_j} + \frac{1}{2}\boldsymbol{u}_j^T \frac{\partial \boldsymbol{K}_j}{\partial E_j}\boldsymbol{u}_j + \boldsymbol{\lambda}_j^T \frac{\partial \boldsymbol{K}_j}{\partial E_j}\boldsymbol{u}_j + \boldsymbol{\lambda}^T \left(\boldsymbol{K}\frac{\partial \boldsymbol{u}}{\partial E_j} - \frac{\partial \boldsymbol{F}}{\partial E_j} \right) \tag{39}$$

where $\boldsymbol{u}_j$ and $\boldsymbol{\lambda}_j$ are respectively the displacement vector and adjoint variable vector corresponding to element j. The force vector is independent of Young's moduli, i.e., $\frac{\partial \boldsymbol{F}}{\partial E_j} = \boldsymbol{0}$. We eliminate the state variable gradients $\frac{\partial \boldsymbol{u}}{\partial E_j}$ from Eq. (38) by using the adjoint equation,

$$\begin{aligned} &\boldsymbol{K}\boldsymbol{\lambda} + \boldsymbol{K}\boldsymbol{u} = \boldsymbol{0} \\ &\Rightarrow \boldsymbol{\lambda} = -\boldsymbol{u} \end{aligned} \tag{40}$$

We can see from Eq. (40) that the adjoint variables $\boldsymbol{\lambda}$ are proportional to the state variables $\boldsymbol{u}$, and so the mean compliance function is called self-adjoint. Substituting the adjoint variables in Eq. (40) into Eq. (39) and using the definition of stiffness matrix in Eq. (32), the sensitivities for mean-compliance in the absence of design-dependent loads are given by

$$\begin{aligned} \frac{\partial C}{\partial \rho_{jk}} &= \left(-\frac{1}{2}\boldsymbol{u}_j^T \frac{\partial \boldsymbol{K}_j}{\partial E_j}\boldsymbol{u}_j \right) \cdot \frac{\partial E_j}{\partial \rho_{jk}} \\ &= \left(-\frac{1}{2}\boldsymbol{u}_j^T \left[\int_{\Omega_j} \boldsymbol{B}_j^T \bar{\boldsymbol{D}} \boldsymbol{B}_j \; d\Omega \right] \boldsymbol{u}_j \right) \cdot \frac{\partial E_j}{\partial \rho_{jk}} \end{aligned} \tag{41}$$

where $\bar{\boldsymbol{D}}$ is the material elasticity tensor with unit Young's modulus. The sensitivities of Young's modulus are given using the extended SIMP interpolation in Eq. (6) as

$$\frac{\partial E_j}{\partial \rho_{jk}} = -p\rho_{jk}^{p-1}\left[\prod_{t=1}^{k-1}\rho_{jt}^{p}\right]E_{s_{k-1}} + \sum_{l=k+1}^{N_m}\left(1-\rho_{jl}^{p}\right)\left[\prod_{\substack{t=1\\t\neq k}}^{l-1}\rho_{jt}^{p}\right]p\rho_{jk}^{p-1}E_{s_{l-1}} + p\rho_{jk}^{p-1}\left[\prod_{\substack{t=1\\t\neq k}}^{N_m}\rho_{jt}^{p}\right]E_{s_{N_m}} \tag{42}$$

The sensitivities of the mass of the structure can be computed in terms of the mass density derivatives as

$$\frac{\partial w(\boldsymbol{\rho})}{\partial \rho_{jk}} = \frac{\partial w}{\partial \gamma_j}\cdot\frac{\partial \gamma_j}{\partial \rho_{jk}} = V_j\cdot\frac{\partial \gamma_j}{\partial \rho_{jk}} \tag{43}$$

where the sensitivities of the mass density of an element are derived using the extended SIMP interpolation,

$$\frac{\partial \gamma_j}{\partial \rho_{jk}} = \left[\prod_{t=1}^{k-1}\rho_{jt}\right]\gamma_{s_{k-1}} + \sum_{l=k+1}^{N_m}\left(1-\rho_{jl}\right)\left[\prod_{\substack{t=1\\t\neq k}}^{l-1}\rho_{jt}\right]\gamma_{s_{l-1}} + \left[\prod_{\substack{t=1\\t\neq k}}^{N_m}\rho_{jt}\right]\gamma_{s_{N_m}} \tag{44}$$

where $\gamma_{s_0} = 0$, the void material. The sensitivities for mean compliance in Eq. (41) are valid when there are no design-dependent loads acting on the design domain. When we consider the effect of design dependent self-weight loads, the force vector in Eq. (31) depends on the design variables via the mass density (see Eq. (35)). This means the third term in Eq. (38) is nonzero in the presence of self-weight loads. The mean compliance sensitivities in the presence of self-weight loads are thus given by

$$\frac{\partial C}{\partial \rho_{jk}} = \left(-\frac{1}{2}\boldsymbol{u}_j^T\left[\int_{\Omega_j}\boldsymbol{B}_j^T\bar{\boldsymbol{D}}\boldsymbol{B}_j\,d\Omega\right]\boldsymbol{u}_j\right)\cdot\frac{\partial E_j}{\partial \rho_{jk}} + \frac{\partial \gamma_j}{\partial \rho_{jk}}\boldsymbol{u}_j^T\int_{\Omega_j}\boldsymbol{N}_j^T\boldsymbol{g}\,d\Omega \tag{45}$$

where the sensitivities of the mass densities are computed using Eq. (44).

We now consider the applications with design-dependent hydrostatic pressure loads. The fluid–structure interface changes when an element on the boundary of the structure at any iteration changes from solid to void state (or vice-versa). The first term in the chain rule expression in Eq. (38) is nonzero in the presence of hydrostatic pressure loads (see Eq. (34)). We use a semi-analytical approach to arrive at the sensitivities of the force vector in the presence of hydrostatic pressure loads. We should note that only the first column of design variables in $\boldsymbol{\rho}$ has nonzero sensitivities for the pressure loads. This is because only the first column of design variables causes the presence of any solid material in the elements, which in turn indicates the action of pressure loading on the boundaries of elements. Fig. 2 shows the surface pressure loads on an element e when the element changes from solid state to fluid state. The gradients of the force vector are just given by difference between the force vectors in the two scenarios as shown in Fig. 2(c). The force vector on element e in Fig. 2(c) gives the sensitivities of pressure loading with respect to ρ_{e1}. Using Eq. (34), the sensitivities of mean compliance in the presence of only design dependent pressure loads are given by

$$\frac{\partial C}{\partial \rho_{jk}} = \left(-\frac{1}{2}\boldsymbol{u}_j^T\left[\int_{\Omega_j}\boldsymbol{B}_j^T\bar{\boldsymbol{D}}\boldsymbol{B}_j\,d\Omega\right]\boldsymbol{u}_j\right)\cdot\frac{\partial E_j}{\partial \rho_{jk}} + \delta_{k1}\boldsymbol{u}_j^T\left[\sum_{b\in\Gamma_j}\int_{\Gamma_b}\boldsymbol{G}_b^T\boldsymbol{n}_b\,d\Gamma\right] \tag{46}$$

where δ_{xy} is the Kronecker delta function,

$$\delta_{xy} = \begin{cases} 1 & : x = y \\ 0 & : x \neq y \end{cases} \tag{47}$$

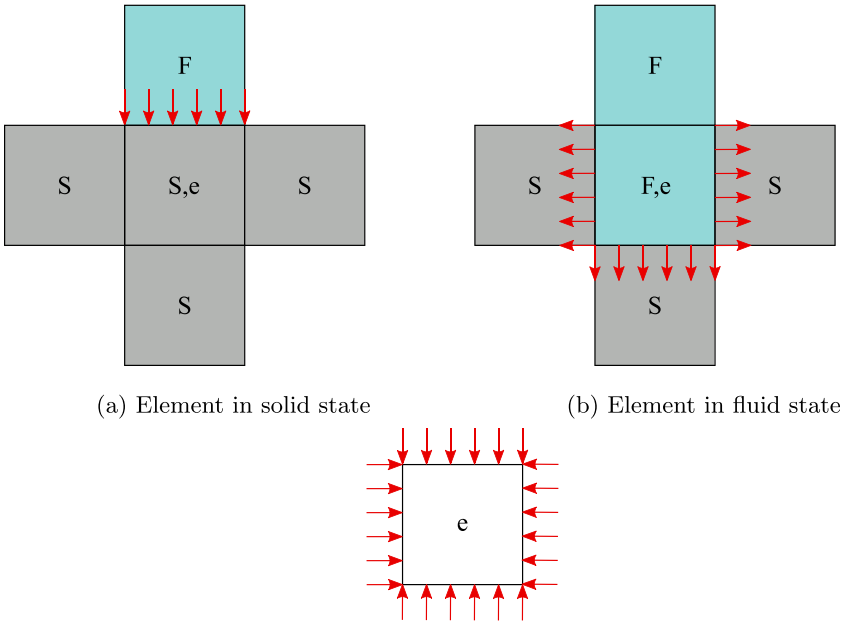

(a) Element in solid state (b) Element in fluid state

(c) Finite-Difference of the pressure loads

Fig. 2. Computation of semi-analytical sensitivities for the pressure loads on element e(S→ Structure, F→ Fluid).

Using Eqs. (45) and (46), the sensitivities of mean compliance in the presence of both design-dependent pressure loads and design-dependent self-weight loads are given by

$$\frac{\partial C}{\partial \rho_{jk}} = \left(-\frac{1}{2}\boldsymbol{u}_j^T\left[\int_{\Omega_j} \boldsymbol{B}_j^T \bar{\boldsymbol{D}} \boldsymbol{B}_j \, d\Omega\right]\boldsymbol{u}_j\right) \cdot \frac{\partial E_j}{\partial \rho_{jk}} + \delta_{k1}\boldsymbol{u}_j^T\left[\sum_{b\in\Gamma_j}\int_{\Gamma_b} \boldsymbol{G}_b^T \boldsymbol{n}_b \, d\Gamma\right] + \frac{\partial \gamma_j}{\partial \rho_{jk}}\boldsymbol{u}_j^T \int_{\Omega_j} \boldsymbol{N}_j^T \boldsymbol{g} \, d\Omega \tag{48}$$

The sensitivities derived in this section are filtered and then the integer linear suboptimization problem in Eq. (27) is generated and solved using an ILP solver.

5.1. Sensitivity filtering

The stresses and strains are discontinuous across elements when C^0 finite elements are used (as in this work). Such finite elements exhibit artificially high stiffness when two finite elements just have a nodal hinge-like connectivity. This spuriousness leads to checkerboards in the optimized topology [54]. We use sensitivity filtering to smoothen the noisy sensitivities and avoid checkerboarding in structural optimization. Sensitivity filtering also helps in achieving mesh-independent solutions. We use a mesh-independent sensitivity filter [39] for this purpose.

A nodal sensitivity field is generated from the elemental sensitivities by averaging the neighboring element sensitivities at each node,

$$\frac{\partial f}{\partial y_{nj}} = \frac{1}{|E|}\sum_{e\in E}\frac{\partial f}{\partial \rho_{ej}} \qquad j \in [1, \ N_m] \tag{49}$$

where y_{nj} is the nodal design variable corresponding to the jth material and nth node, $|E|$ is the cardinality of the set E of the neighboring elements to a node n. Fig. 3(a) shows a couple of nodes with the corresponding sets with neighboring elements whose sensitivities are averaged in Eq. (49). The filtered sensitivity field is obtained using a

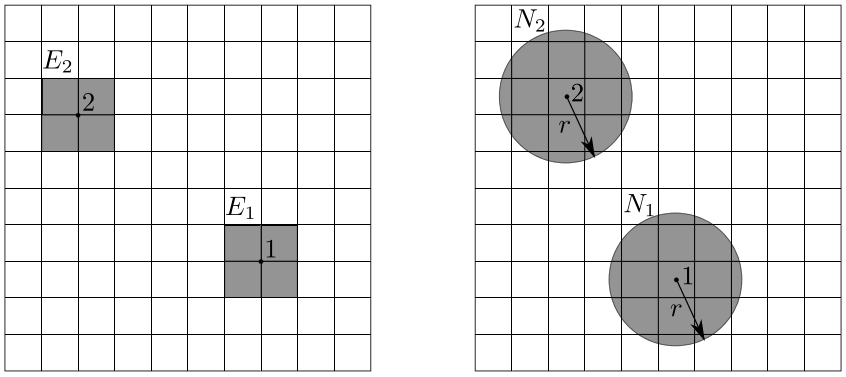

(a) Nodes 1 and 2 (b) Elements 1 and 2

Fig. 3. Filtering — Areas of averaging for nodal and filtered elemental sensitivities.

weighted averaging of sensitivities at the neighboring nodes,

$$\frac{\partial f}{\partial \rho_{ej}} \longleftarrow \frac{\sum_{n\in N} \alpha_{en} \cdot \dfrac{\partial f}{\partial y_{nj}}}{\sum_{n\in N} \alpha_{en}} \qquad j \in [1,\ N_m] \tag{50}$$

where N is the set of neighboring nodes to an element e (e.g. Fig. 3(b)) and α_{en} are the weights used for averaging,

$$\alpha_{en} = \texttt{max}\big(0,\ r - \texttt{dist}(\boldsymbol{x}_{ce},\ \boldsymbol{x}_n)\big) \tag{51}$$

where $\texttt{dist}(\cdot\ ,\ \cdot)$ is the Euclidean distance function, r is the radius of a circular region (2D) or a spherical region (3D) surrounding the element e (see Fig. 3(b)), and $\boldsymbol{x}_{ce}$ and $\boldsymbol{x}_n$ are the coordinates of the centroid of element e and node n respectively. The weights are higher for nodes closer to the element e as compared to the nodes farther from the element. The sensitivities obtained through sensitivity analysis are filtered using the mesh-independent filter and are used in the suboptimization problems (Eq. (27)).

6. Examples

In this section, we show few examples of multimaterial structural optimization solved using the TOBS method as described in the previous sections. All the examples are two-dimensional and the meshes contain unit plane-stress quadrilateral finite elements. The void elements in the design domain are handled during FEA using a soft-kill approach. The Poisson's ratio of all the materials considered in this work is the same, $\nu = 0.3$.

6.1. Compliance minimization

We show some examples of multimaterial compliance minimization subject to a mass constraint. A mass constraint usually helps in yielding a better optimal design as compared to one volume constraint per material used [55], because if one were to use separate volume constraints for the material phases, the constraint bounds are nontrivial to choose. We consider two materials for structural optimization: material-1 with Young's modulus 0.6 and mass density 0.4, and material-2 with Young's modulus 1.0 and mass density 1.0. The parameters used for structural optimization are $\epsilon = 0.02$, $\beta = 0.05$, and $r = 2$ finite elements. The initial design domain (with mass w_i used is the fully solid domain made of the stiffest material available for optimization. The upper limit on mass is specified as a factor of this initial mass w_i.

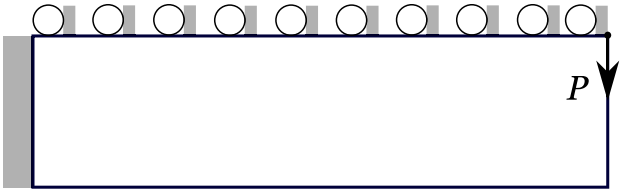

Fig. 4. Cantilever Beam — Design Domain with boundary conditions and loads.

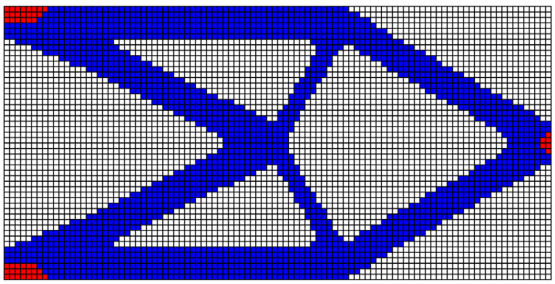

(a) Optimized topology

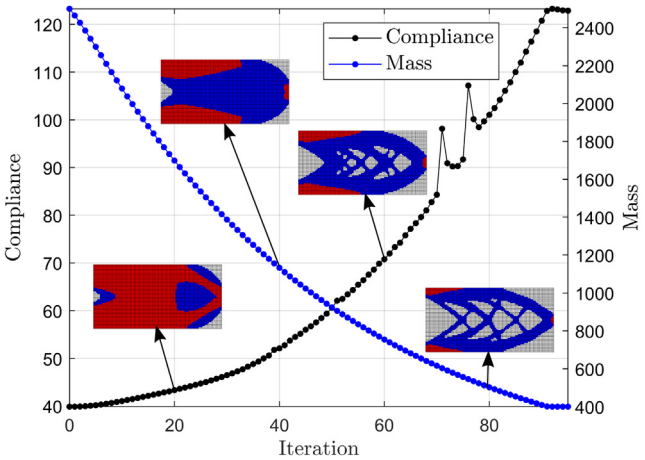

(b) Convergence history

Fig. 5. Cantilever Beam — Compliance minimization subject to $m \leq 0.16 \cdot w_i$
(blue → material-1, red → material-2). (For interpretation of the references to color in this figure legend, the reader is referred to the web version of this article.)

6.1.1. Cantilever beam

The compliance minimization of a cantilever beam subject to a mass constraint is considered using the lower half of the design domain, owing to the (anti) symmetry of the problem. The boundary conditions and loads applied to the design domain are shown in Fig. 4. The beam is clamped on the left edge, with a point load on the right end. Antisymmetry boundary conditions are applied on the top edge of the design domain preventing the horizontal displacement of the top edge of the design domain.

The design domain is meshed using 100×25 elements, and the loading is $P = 1$. The upper bound for the mass constraint is $0.16 \cdot w_i$. The optimized topology and convergence history are shown in Fig. 5. The convergence history also shows some intermediate solutions. In the initial iterations, material is removed at the right corners

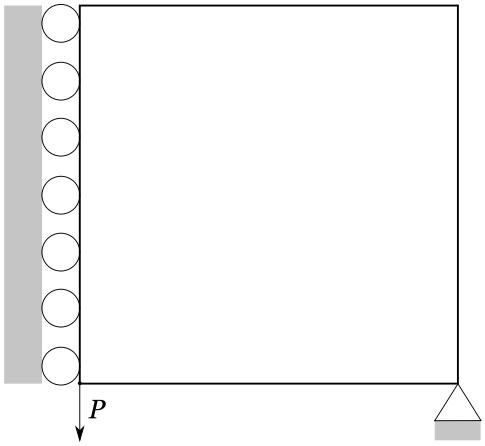

Fig. 6. Michell Structure — Design Domain with boundary conditions and loads.

of the design domain where rigid body motion is dominant. The less stressed elements change from material-2 to the lighter material-1. The final topology includes stiffer material-2 around the load point on the right edge and the reaction force location on the clamped edge. The convergence history shows a smooth convergence to the final solution after 97 iterations.

6.1.2. Michell structure

We design the topology of a Michell structure using compliance minimization subject to a mass constraint. Owing to symmetry, we use only the right half of the design domain. The pertinent loads and boundary conditions on the design domain are showed in Fig. 6. The structure is pin-supported on the bottom right corner and symmetric boundary conditions are applied on the left edge of the design domain. A point load is applied on the left bottom corner of the design domain.

The design domain is meshed using 100×100 elements, and the loading is $P = 1$. The upper bound for the mass constraint is $0.16 \cdot w_i$. The optimized topology and the convergence history are shown in Fig. 7. The topologies at the intermediate iterations show that material gets removed where rigid body motion is dominant, and the lesser stressed areas change from the heavier material-2 to the lighter material-1. The final solution contains the stiffer and heavier material-1 only around the load point and around the pin joint to better handle the loading on the structure whilst keeping the structural mass low. The convergence history shows a smooth convergence to the final topology after 97 iterations.

The Michell structure is now designed with different material elastic properties such that the difference between the Young's moduli of the two materials considered is much larger, whilst the mass densities remain the same. The mass constraint considered is $0.20 \cdot w_i$. Three optimized topologies for different material elastic properties are shown in Fig. 8. The optimized topologies for the material elastic properties $\{0.06,\ 1.0\}$ and $\{0.6,\ 10.0\}$ are the same because the objective function values of both topology optimization problems at all iterations are scalar multiples of each other. This means the evolution of topologies is the same in both cases. We can also observe that the optimized structures Fig. 8(a) and Fig. 8(c) are made completely of the much stiffer material-2, since it is not only much stiffer, but also its mass density is not much higher than that of the very flexible material-1. When the elastic moduli of the materials are not very disparate, as observed in Fig. 8(b), both material-1 and material-2 are seen arranged in the optimized structure according to the loading requirements. This example also shows the effectiveness of TOBS method in multimaterial optimization where the available materials have disparate elastic properties.

6.1.3. MBB beam

A two-material Messerschmitt–Bölkow–Blohm (MBB) beam is designed using the TOBS method. Only the right half of the model is considered due to the symmetry. The design domain with loads and boundary conditions is

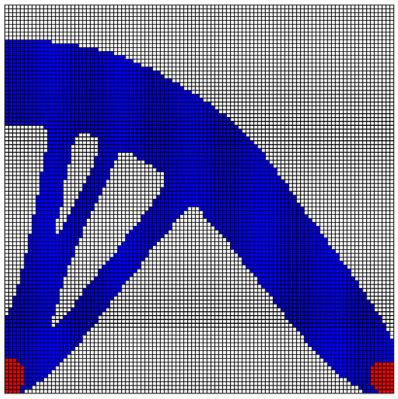

(a) Optimized topology

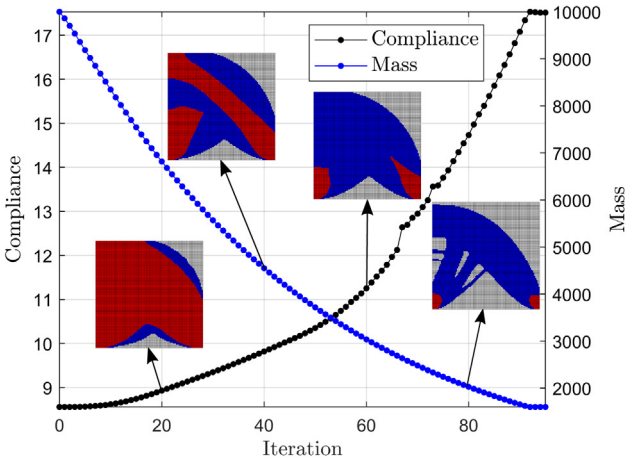

(b) Convergence history

Fig. 7. Michell Structure — Compliance minimization subject to $m \leq 0.16 \cdot w_i$
(blue → material-1, red → material-2). (For interpretation of the references to color in this figure legend, the reader is referred to the web version of this article.)

shown in Fig. 9. A vertical point load is applied on the top of the beam on the left edge, with a roller support on the right corner and symmetric boundary conditions on the left edge.

The design domain is meshed using 120×40 elements, and the loading is $P = 1$. The upper bound for the mass constraint is $0.20 \cdot w_i$. The optimized topology and convergence history with the evolution of topologies are shown in Fig. 10. The spikes in convergence correspond to member breaks. As in the previous examples, void material is seen at locations where rigid body motion is dominant in the design domain, material-2 is seen at the load point, and the reaction force locations, and the lighter material-1 is seen elsewhere.

The MBB beam is now designed with different upper bounds for the mass constraint: $0.15 \cdot w_i$ and $0.25 \cdot w_i$. The corresponding optimized topologies are shown in Fig. 11. Comparing these topologies with the optimized topology for $m \leq 0.20 \cdot w_i$ in Fig. 10, we can see that for $m \leq 0.15 \cdot w_i$, the members just get thinner, and for $m \leq 0.25 w_i$, more members supporting the loads can be seen because of more mass being available for design. The amount of the heavier and stiffer material-2 in the optimized topologies is seen to increase with the upper bound used for the mass constraint.

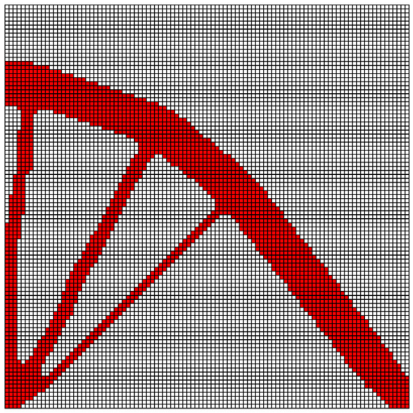

(a) $E_1 = 0.06,\ E_2 = 1.0$ and $E_1 = 0.6,\ E_2 = 10.0$

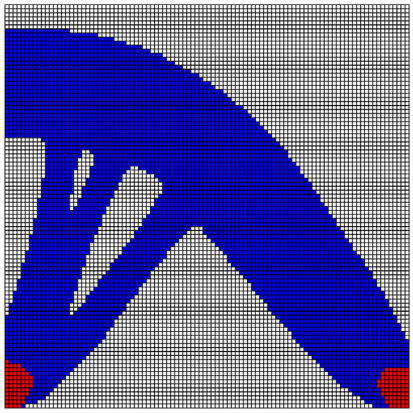

(b) $E_1 = 0.6,\ E_2 = 1.0$

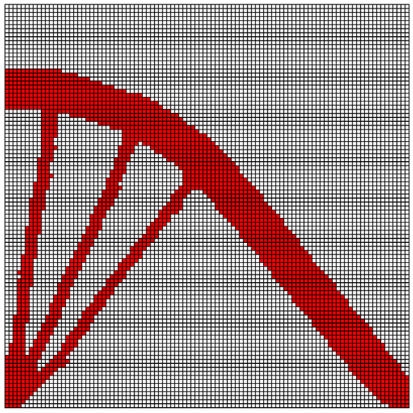

(c) $E_1 = 0.06,\ E_2 = 10.0$

Fig. 8. Michell Structure — Compliance minimization with different elastic properties (blue → material-1, red → material-2). (For interpretation of the references to color in this figure legend, the reader is referred to the web version of this article.)

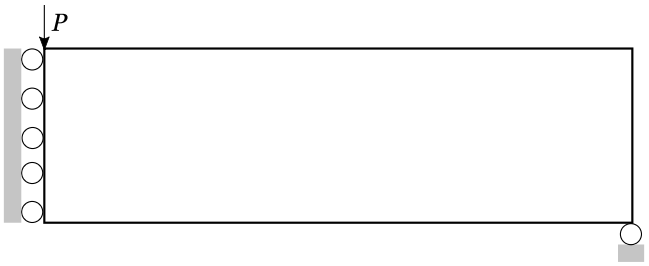

Fig. 9. MBB Beam — Design Domain with boundary conditions and loads.

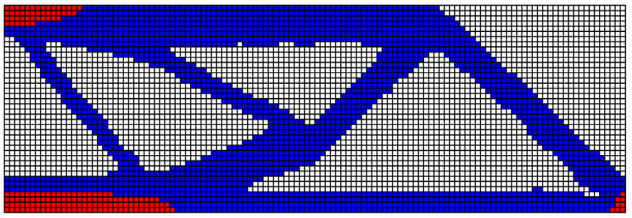

(a) Optimized topology

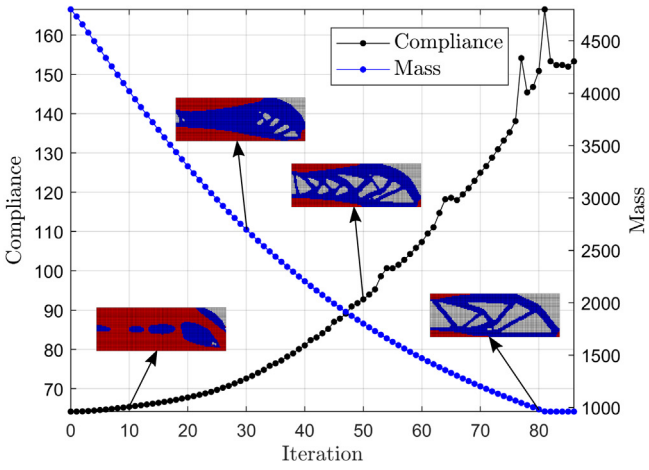

(b) Convergence history

Fig. 10. MBB Beam — Compliance minimization subject to $m \leq 0.20 \cdot w_i$
(blue → material-1, red → material-2). (For interpretation of the references to color in this figure legend, the reader is referred to the web version of this article.)

6.2. Mass minimization

We now optimize multimaterial structures using mass minimization subject to a compliance constraint, for the same design domains used in compliance minimization. Topology optimization using mass minimization is more practical since an engineer aims to design as light-weight structure as possible whilst satisfying some performance requirements (in this case, the compliance constraint). The two materials used for optimization are the same as that of compliance minimization (Section 6.1). The optimization parameters used are $\epsilon = 0.01$, $\beta = 0.05$, and $r = 2$

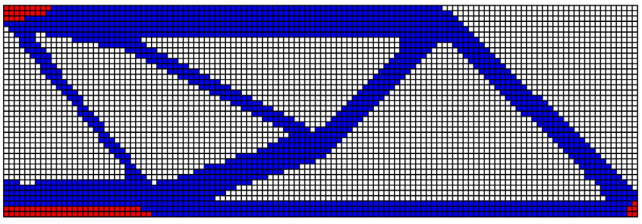

(a) $m \leq 0.16 \cdot w_i$

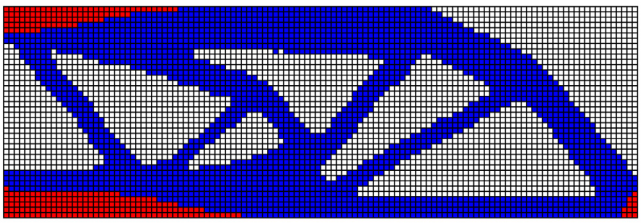

(b) $m \leq 0.25 \cdot w_i$

Fig. 11. MBB Beam — Compliance Minimization for different bounds for the mass constraint (blue → material-1, red → material-2). (For interpretation of the references to color in this figure legend, the reader is referred to the web version of this article.)

finite elements. The initial solution used is the fully solid domain filled with the stiffer material. The upper bound for the compliance constraint is specified as a factor of the compliance C_i of the initial solution.

6.2.1. Cantilever beam

The domain (Fig. 4) is meshed with 100 × 25 elements. The mass of the beam is minimized subject to an upper bound $3.0 \cdot C_i$ on the compliance constraint. The optimized topology and the convergence history with some intermediate solutions are shown in Fig. 12. The optimized structure looks topologically similar to the compliance minimization example (Fig. 5) discussed in Section 6.1. The stiffer material-2 is located near loading and reaction force locations, but is used frugally by the optimizer because material-2 is heavier. The convergence history shows the convergence of the compliance constraint as a factor of the compliance C_i of the initial solution. The convergence history and the intermediate topologies indicate smooth convergence to the optimized solution after 137 iterations.

6.2.2. Michell structure

The design domain (Fig. 6) is meshed with 100 × 100 elements. The mass of the beam is minimized subject to an upper bound $2.0 \cdot C_i$ on the compliance constraint. The results of structural optimization: the final topology, the convergence history and a few intermediate solutions are shown in Fig. 13. The convergence to final topology is observed to be smooth after 144 iterations. The stiffer material-2 is concentrated near the loading and reaction force locations, and rest of the optimal topology is made of material-1, since it is lighter than material-2.

The same example is now investigated when different material mass densities are used. Fig. 14 shows the final topologies when different sets of material mass densities are used where the structures are optimized using mass minimization subject to a compliance constraint of $3.0 \cdot C_i$ (also see Fig. 13). The material elastic properties are unchanged, however. The optimized topologies for the cases with mass densities {0.04, 1.0} and {0.4, 10.0} are the same because the objective functions in both cases are just scalar multiples of each other. We can observe that compared to Fig. 13, the optimized topologies in Fig. 14 have more material-1, because the density of material-1 is much lower than that of material-2. The topology in Fig. 14(a) has almost no material-2 (just 6 elements) because of it being much heavier than material-1, whilst the elastic moduli of both the materials are of the same order. The

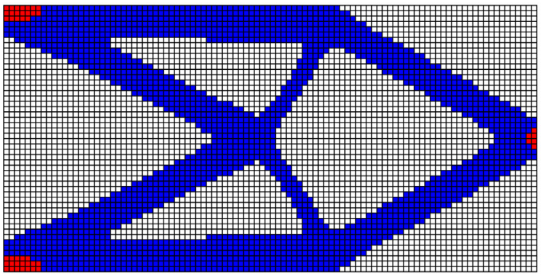

(a) Optimized topology

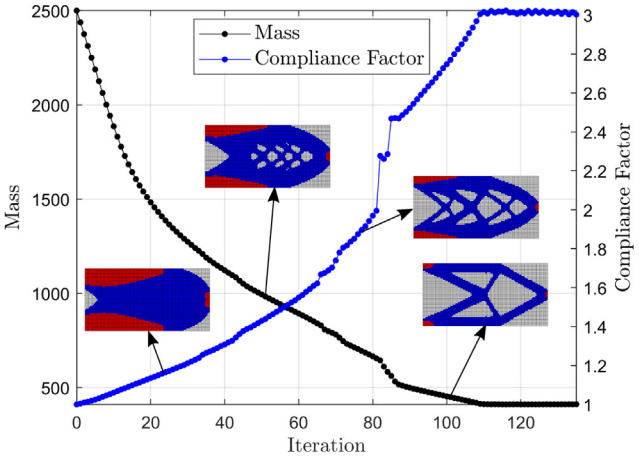

(b) Convergence history

Fig. 12. Cantilever Beam — Mass minimization subject to $C \leq 3.0 \cdot C_i$
(blue → material-1, red → material-2). (For interpretation of the references to color in this figure legend, the reader is referred to the web version of this article.)

topology with mass densities $\{0.04, 10.0\}$ in Fig. 14 is observed to be made completely of material-1, because of it being relatively much lighter whilst being decently stiffer to satisfy the compliance constraint.

6.2.3. MBB beam

The design domain (Fig. 9) is meshed with 120×40 elements. The mass of the beam is minimized subject to an upper bound $2.0 \cdot C_i$ on the compliance constraint. The final topology and the convergence history are shown in Fig. 13. A smooth convergence to the optimized topology after 81 iterations is observed. As in the previous examples, the stiffer material-2 is concentrated near loading and reaction force locations, and the rest of the final topology is made of the lighter material-1.

These examples demonstrate that the TOBS framework is effective in multimaterial optimization, not only in compliance minimization but also in mass minimization.

6.3. Design-dependent loads

We apply the TOBS method for multimaterial structural optimization in the presence of design-dependent loads. We design optimized topologies using compliance minimization subject to a mass constraint in the presence of design-dependent hydrostatic pressure loads and design-dependent self-weight loads. We investigate the arch structure design and piston design using two and three materials for optimization. The optimization parameters used

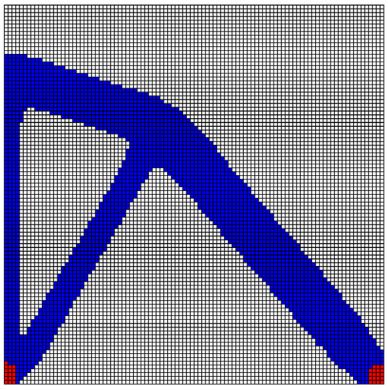

(a) Optimized topology

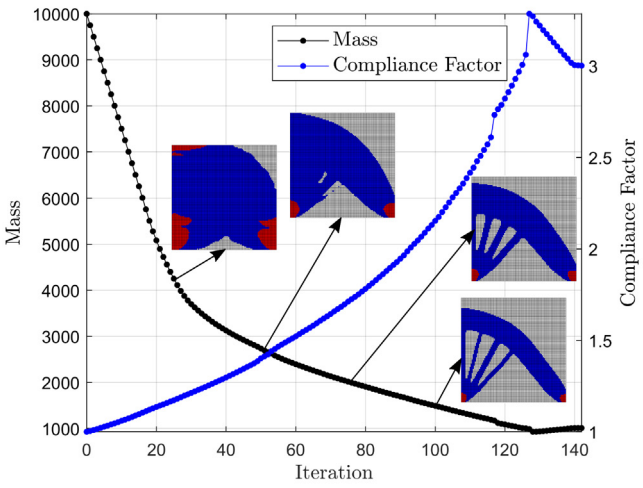

(b) Convergence history

Fig. 13. Michell Structure — Mass minimization subject to $C \leq 3.0 \cdot C_i$
(blue → material-1, red → material-2). (For interpretation of the references to color in this figure legend, the reader is referred to the web version of this article.)

are $\epsilon = 0.01$, $\beta = 0.05$ and $r = 2$ finite elements. The upper bound for the mass constraint is specified as a factor of the mass w_i of the initial solution. The self-weight in each finite element is constant and is specified proportional to the mass density of the material γ_e associated with the element, and the load acts vertically downwards.

6.3.1. Arch structure

An arch-like structure is designed using compliance minimization, subject to a mass constraint of $0.15 \cdot w_i$. A unit hydrostatic pressure load is applied on the fluid–structure boundary of the topology at every iteration. Since the fluid–structure boundary changes each iteration, this is an example where design-dependent surface loads are in action. The symmetric part of the design domain with the pertinent boundary conditions and the surrounding fluid is shown in Fig. 16.

Fig. 17 shows the optimized topology and convergence history when two materials: material-1: $\{E \to 0.6,\ \gamma \to 0.4\}$ and material-2: $\{E \to 1.0,\ \gamma \to 1.0\}$ are made available for optimization. Fig. 18 shows the optimized topology and convergence history when three materials: material-1: $\{E \to 0.6,\ \gamma \to 0.4\}$, material-2: $\{E \to 0.8,\ \gamma \to 0.6\}$

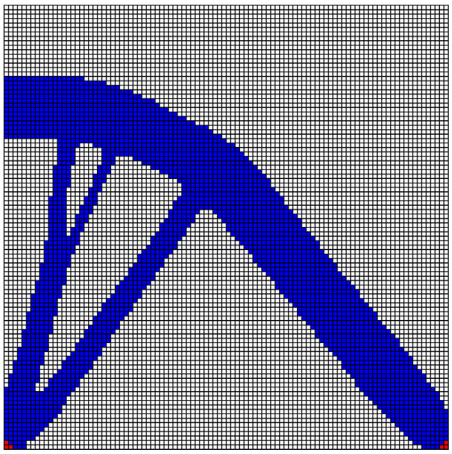

(a) $m_1 = 0.04,\ m_2 = 1.0$ and $m_1 = 0.4,\ m_2 = 10.0$

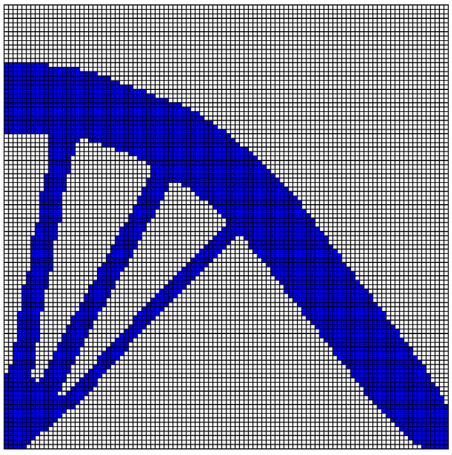

(b) $m_1 = 0.04,\ m_2 = 10.0$

Fig. 14. Michell Structure — Mass minimization with different densities (blue → material-1, red → material-2). (For interpretation of the references to color in this figure legend, the reader is referred to the web version of this article.)

and material-3: $\{E \to 1.0,\ \gamma \to 1.0\}$ are made available for optimization. Both Figs. 17 and 18 show that the stiffer materials are concentrated around pin joint where reaction forces act on the structure. In the three-materials case (Fig. 18), the material-2 is seen around the stiffer material-3 which is seen near the pin joint. The final structure in both cases is an arch-like structure with stiff materials at the pin joint and the lighter material-1 is predominantly seen in the final arch-like topology.

We now design the arch-like structure when both design-dependent pressure loads and design-dependent self-weight loads act on the structure when two and three materials are made available for optimization. The self-weight load applied is $0.10 \cdot \gamma_e$, acting vertically downwards. Figs. 19 and 20 show the optimal topologies and convergence histories for the cases with two and three materials respectively. The materials properties used are the same as those used above in the problems with just pressure loads, Fig. 17 and Fig. 18 respectively. Comparing with the optimized topologies obtained without applying self-weight loads (Figs. 17 and 18), we can observe that the

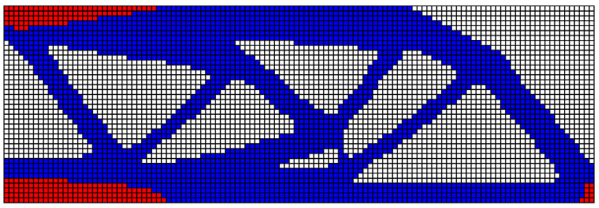

(a) Optimized topology

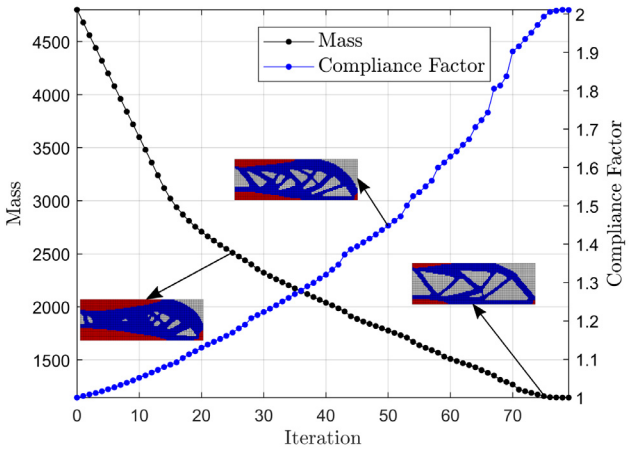

(b) Convergence history

Fig. 15. MBB Beam — Mass minimization subject to $C \leq 2.0 \cdot C_i$
(blue → material-1, red → material-2). (For interpretation of the references to color in this figure legend, the reader is referred to the web version of this article.)

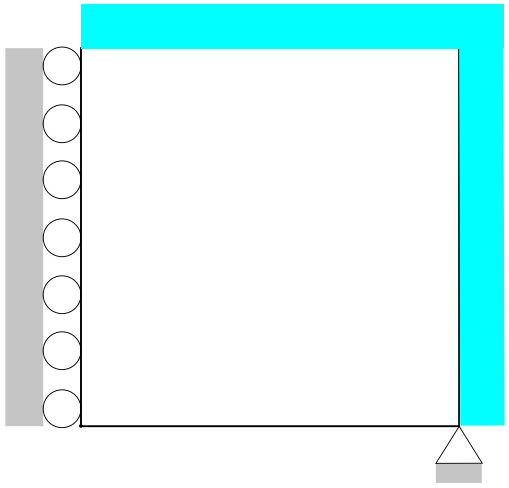

Fig. 16. Arch Structure — Design Domain with boundary conditions and surrounding fluid.

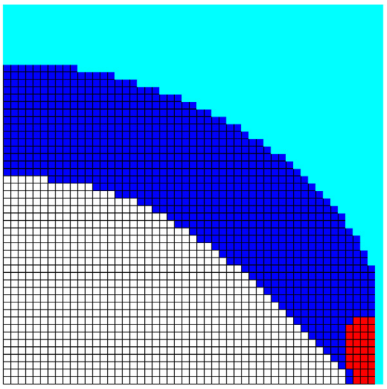

(a) Optimized topology

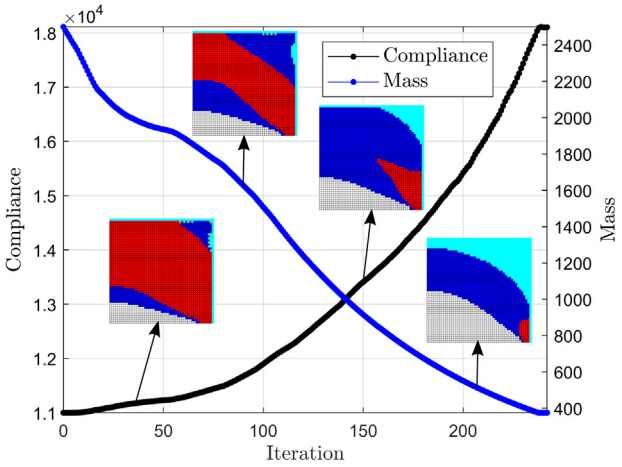

(b) Convergence history

Fig. 17. Arch Structure — Compliance minimization subject to $m \leq 0.15 \cdot w_i$ in the presence of design-dependent pressure loads (blue → material-1, red → material-2). (For interpretation of the references to color in this figure legend, the reader is referred to the web version of this article.)

topologies optimized in the presence of both pressure and self-weight loads have the arch thinner on the left top corner and are thicker near the stiffer material(s) at the bottom right corner. This is because lesser material at the top left corner reduces bending strains in the arch owing to the self-weight loading. The one compliance oscillation in the convergence history in Fig. 20 is because of some floating mass which leads to high compliance because of self-weight loading, and this mass disappears in the next iteration. The convergence curves show smooth convergence to the optimized solution. Unlike optimization without self-weight loads where pressure loads cause more compliance with decrease in mass, compliance can decrease with decreasing mass, because the extent of self-weight loading decreases with decrease in mass.

We should note that for optimization with too high self-weight loading as compared to pressure loads, the optimized structure is an empty structure because no solid elements imply no large strains due to self-weight. The optimization in this scenario can be broadly divided into two phases: 1. The self-weight loading is dominant and so the compliance drops fast as the mass decreases, 2. The pressure loading dominates preventing the optimizer from obtaining an empty structure as optimized solution, and the compliance increases because of the pressure loads. This two-phase phenomenon leads to convergence of optimization when the mass constraint is inactive for some values of its upper bound. We demonstrate this by solving the same optimization problem with upper bounds $0.25 \cdot w_i$ and $0.30 \cdot w_i$ for the mass constraint. The corresponding optimized topology and convergence history when

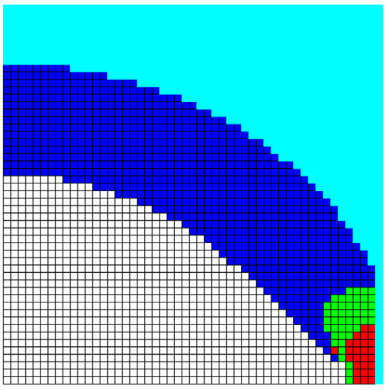

(a) Optimized topology

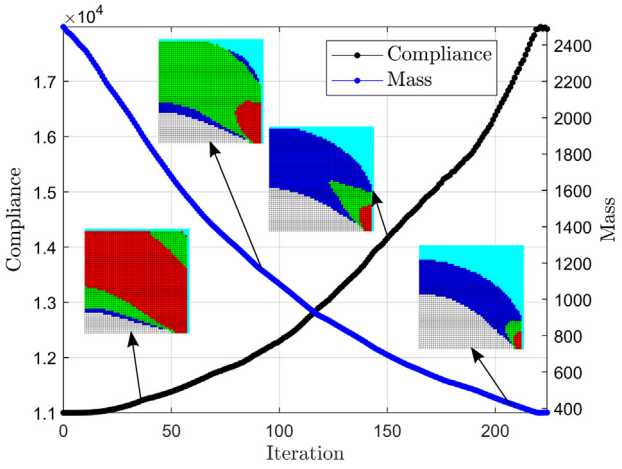

(b) Convergence history

Fig. 18. Arch Structure — Compliance minimization subject to $m \leq 0.15 \cdot w_i$ in the presence of design-dependent pressure loads (blue → material-1, green → material-2, red → material-3). (For interpretation of the references to color in this figure legend, the reader is referred to the web version of this article.)

two and three materials are available for optimization are shown in Figs. 21 and 21 respectively. We can see from Fig. 21 that both for $m \leq 0.25 \cdot w_i$ and $m \leq 0.30 \cdot w_i$, the optimization converges at the same topology at around $0.156 \cdot w_i$. In fact, when any upper bound value above $0.156 \cdot w_i$ is used for optimization, the convergence still happens at the same topology as showed in Fig. 21. This upper bound value of the mass constraint is the point at which pressure loads become more important in the problem than the self-weight loads and the compliance starts increasing with decrease in additional mass. From Fig. 19 corresponding to $0.15 \cdot m_i$ constraint, we can see that the compliance decreases with loss of mass in the initial iterations until the pressure loads become more important than the self-weight loads, after which the compliance increases with loss of mass. The convergence history for $0.30 \cdot m_i$ shows a smooth convergence with the mass constraint being inactive at convergence (Fig. 21). A similar convergence at an inactive mass constraint value is observed in the case of three materials as seen in Fig. 22. The spike in compliance convergence is the same spike observed in Fig. 20 because of the floating mass. This example also shows the effectiveness of TOBS method in dealing with convergence at inactive constraint values.

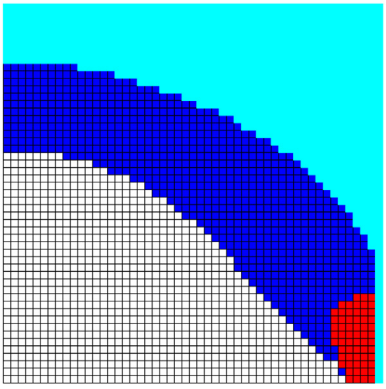

(a) Optimized topology

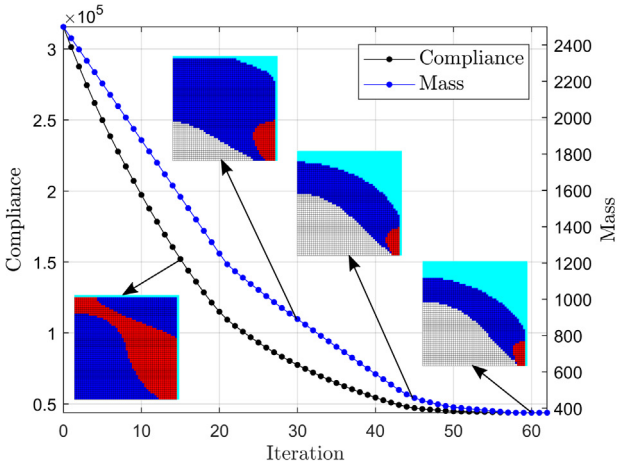

(b) Convergence history

Fig. 19. Arch Structure — Compliance minimization subject to $m \leq 0.15 \cdot w_i$ in the presence of design-dependent pressure and self-weight loads
(blue → material-1, red → material-2). (For interpretation of the references to color in this figure legend, the reader is referred to the web version of this article.)

6.3.2. Piston design

We design a piston using compliance minimization subject to a mass constraint when design-dependent surface pressure loads and design-dependent volumetric self-weight loads are applied. The symmetric part of the design domain with the boundary conditions and surrounding fluid is shown in Fig. 23. We use a mesh of 120 × 80 unit elements to discretize the design domain. The optimization parameters used for the piston design are $\epsilon = 0.01$, $\beta = 0.05$, and $r = 2$ finite elements. We use three materials for piston design: material-1: $\{E \to 0.6,\ \gamma \to 0.4\}$, material-2: $\{E \to 0.8,\ \gamma \to 0.6\}$ and material-3: $\{E \to 1.0,\ \gamma \to 1.0\}$.

Fig. 24 shows the optimal topology when only pressure loads are considered and a mass constraint with an upper bound of $0.15 \cdot w_i$. Stiffer materials are concentrated around the pin joint, and an arch structure supported by members is formed to better handle the pressure loads. The convergence history is observed to be smooth and the optimization ends after 202 iterations. The same example is now solved after adding self-weight loads $0.02 \cdot \gamma_e$ per element acting vertically downwards. Fig. 25 shows the corresponding optimized topology and convergence history. Comparing with the optimized topology in Fig. 24, we can observe that the optimized topology in Fig. 25

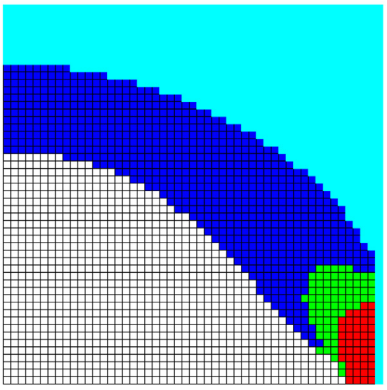

(a) Optimized topology

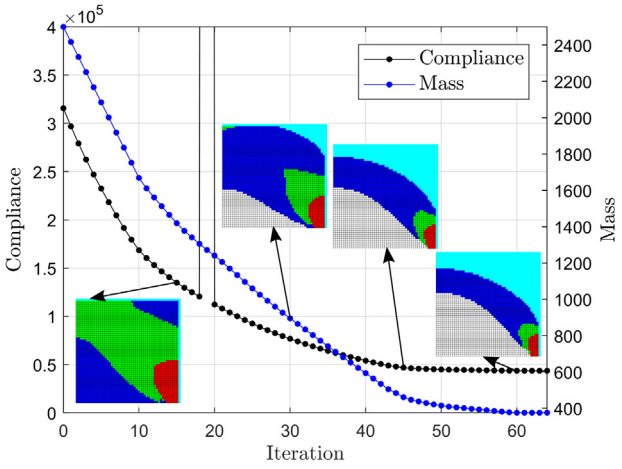

(b) Convergence history

Fig. 20. Arch Structure — Compliance minimization subject to $m \leq 0.15 \cdot w_i$ in the presence of design-dependent pressure and self-weight loads
(blue → material-1, green → material-2, red → material-3). (For interpretation of the references to color in this figure legend, the reader is referred to the web version of this article.)

has a thinner member on the right side of the structure. This is because a thicker member would otherwise induce higher bending strains owing to the self-weight loads. We can also observe at the top right of the structure that the amount of material-2 present in the optimized topology of Fig. 25 is lesser than that of Fig. 24 for the same reason. The spikes in convergence of the compliance are because of floating material (see the first intermediate solution in Fig. 26) in the intermediate iterations which cause high strains because of self-weight loads. Such masses get removed in the very next iterations and the optimization converges smoothly. Similar to the arch structure discussed earlier, this problem can also converge with the mass constraint being inactive. We show the optimized topology and convergence curves for upper bound $0.30 \cdot w_i$ of the mass constraint. We observed that the optimization converges to a topology with around $0.28 \cdot w_i$ mass. The structural optimization with any higher upper bound for mass constraint for this problem converges to this solution (say for e.g. $0.35 \cdot w_i$). This example corroborates the effectiveness of TOBS method in dealing with an inactive constraint by demonstrating smooth convergence.

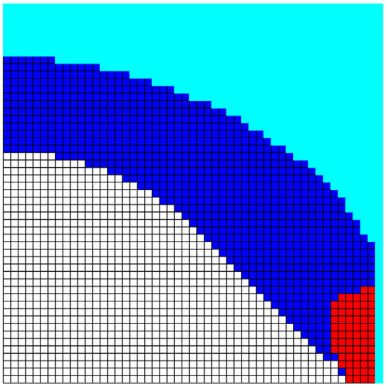

(a) Optimized topology

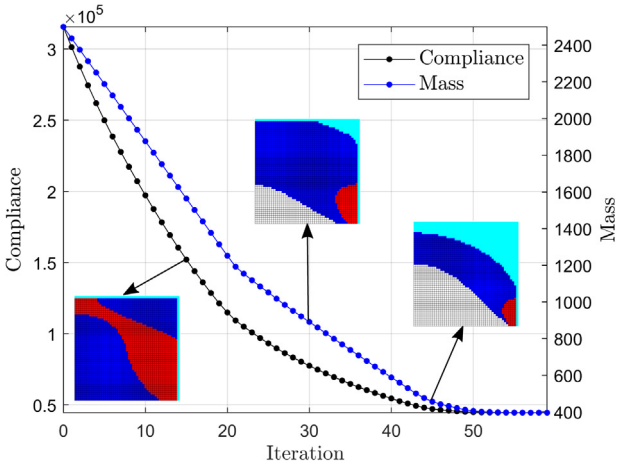

(b) Convergence history

Fig. 21. Arch Structure — Compliance minimization subject to $m \leq 0.30 \cdot w_i$ (or $m \leq 0.25 \cdot w_i$) in the presence of design-dependent pressure and self-weight loads
(blue → material-1, red → material-2). (For interpretation of the references to color in this figure legend, the reader is referred to the web version of this article.)

7. Conclusions

This manuscript designs optimized multi-material structural topologies considering linear elastostatics. We used the extended SIMP interpolation for the Young's modulus and mass density of the material at any point. We used the TOBS method which uses discrete variables and integer linear programming for structural optimization. The sequentially approximated ILP problems are solved using a branch-and-bound solver and the topology is updated until the convergence criterion is satisfied. A new constraint is introduced to regulate the truncation error of the linear approximation. The truncation error-regulating constraint restrains large changes in the total Young's modulus of the structure, maintaining the linear approximation valid. The proposed truncation-error regulating constraint is more accurate for multimaterial problems as compared to that in [23] because it factors in the potential change in the material properties at an element to represent the truncation error. A detailed sensitivity analysis is presented for the pertinent functions used in this work and in various scenarios, like design-dependent pressure loads and design-dependent self-weight loads. Several examples are solved using this novel constraint and a conventional

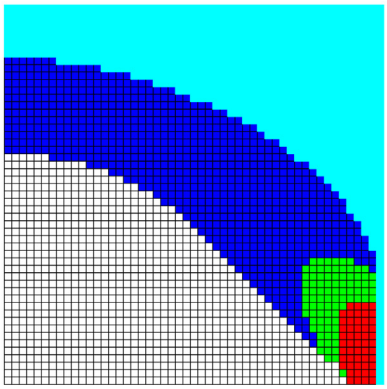

(a) Optimized topology

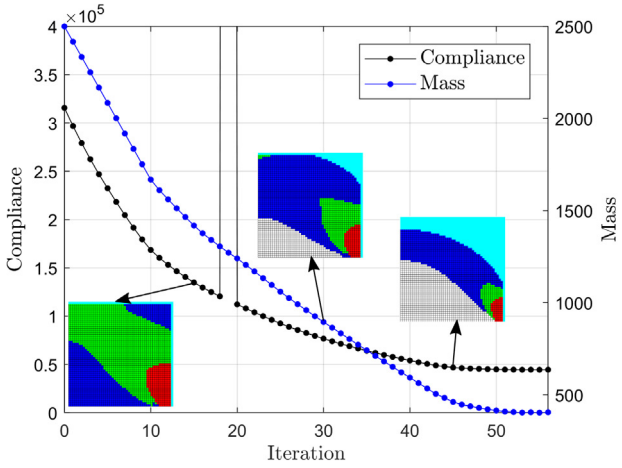

(b) Convergence history

Fig. 22. Arch Structure — Compliance minimization subject to $m \leq 0.30 \cdot w_i$ (or $m \leq 0.25 \cdot w_i$) in the presence of design-dependent pressure and self-weight loads
(blue → material-1, green → material-2, red → material-3). (For interpretation of the references to color in this figure legend, the reader is referred to the web version of this article.)

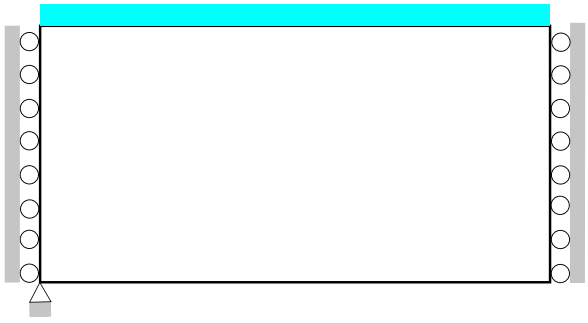

Fig. 23. Piston Design — Design Domain with boundary conditions and surrounding fluid.

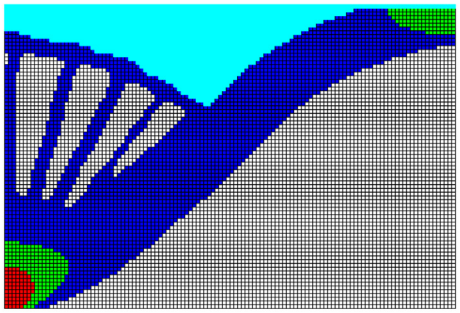

(a) Optimized topology

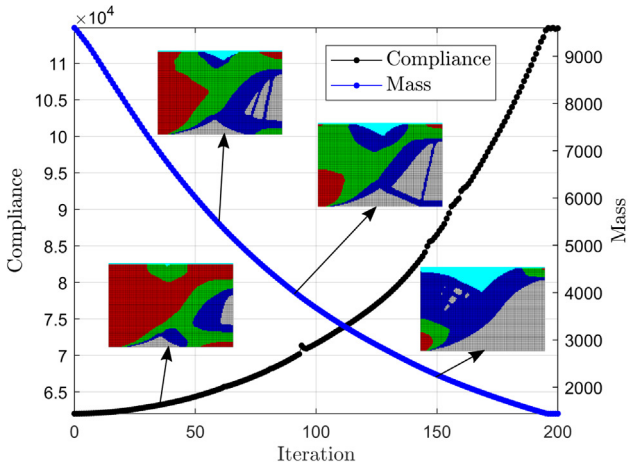

(b) Convergence history

Fig. 24. Piston Design — Compliance minimization subject to $m \leq 0.15 \cdot w_i$ in the presence of design-dependent pressure loads (blue → material-1, green → material-2, red → material-3). (For interpretation of the references to color in this figure legend, the reader is referred to the web version of this article.)

mesh-independent filter is used. Examples showing compliance minimization subject to a mass constraint, as well as mass minimization with respect to a compliance constraint are presented to demonstrate the flexibility and effectiveness of the framework. The discrete structural optimization used in literature for multimaterial problems is BESO, which requires a volume constraint for the design variable-update. The examples considered in this work do not need to include such a constraint, yet yielding optimized discrete multimaterial structures with stable convergence. Examples involving materials with very different Young's moduli are solved to demonstrate the robustness of the framework in solving problems involving very stiff and very flexible elements. Arch and piston structures are designed in the presence of design-dependent pressure loads and design-dependent self-weight loads using two and three materials. A couple of examples is shown where the compliance minimization converges with inactive mass constraint values when both the design-dependent pressure and self-weight loads are acting on the structure. The extent of contribution of both the loads to the mean compliance, and their opposing effects on the mean compliance cause the optimization to stably converge at an constraint values. To the best of authors' knowledge, this is the first work applying a mathematical programming-based discrete structural optimization to

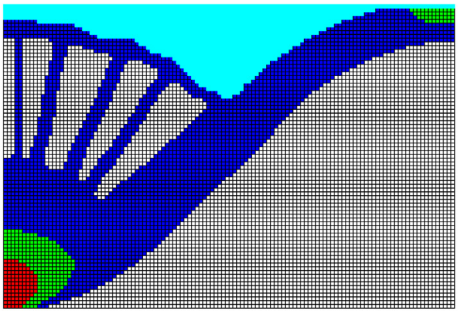

(a) Optimized topology

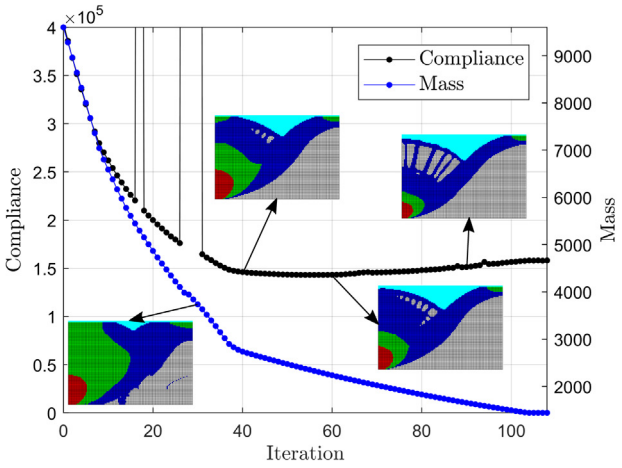

(b) Convergence history

Fig. 25. Piston Design — Compliance minimization subject to $m \leq 0.15 \cdot w_i$ in the presence of design-dependent pressure loads and self-weight loads
(blue → material-1, green → material-2, red → material-3). (For interpretation of the references to color in this figure legend, the reader is referred to the web version of this article.)

multimaterial problems, especially, the problems with pressure loading and inactive constraints. Due to the discrete nature of the topologies, material interface effects can be simply added to the topologies at any iteration, and is a work for the future. It would also be interesting to add material interface size constraints to obtain multimaterial topologies with simpler interfaces for easier manufacturability.

Declaration of competing interest

The authors declare that they have no known competing financial interests or personal relationships that could have appeared to influence the work reported in this paper.

Acknowledgments

The details provided in this manuscript are sufficient to reproduce the results. The code pertinent to this work is available upon request to the corresponding author.

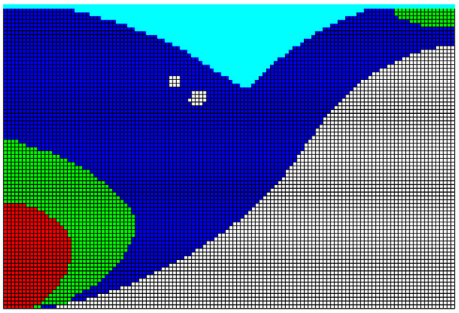

(a) Optimized topology

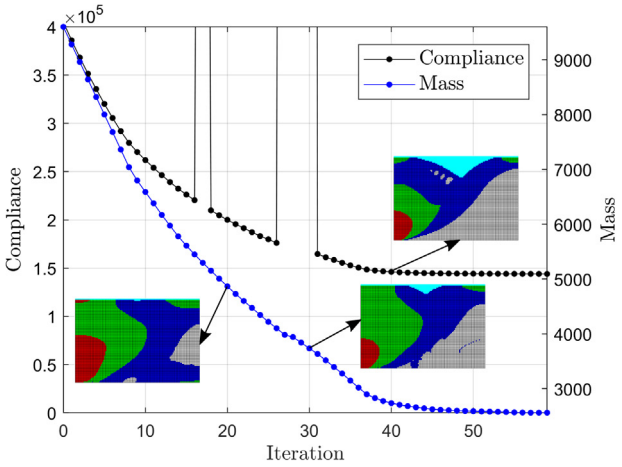

(b) Convergence history

Fig. 26. Piston Design — Compliance minimization subject to $m \leq 0.30 \cdot w_i$ (or $m \leq 0.35 \cdot w_i$) in the presence of design-dependent pressure loads and self-weight loads
(blue → material-1, green → material-2, red → material-3). (For interpretation of the references to color in this figure legend, the reader is referred to the web version of this article.)

References

[1] M.P. Bendse, N. Kikuchi, Generating optimal topologies in structural design using a homogenization method, Comput. Methods Appl. Mech. Engrg. 71 (2) (1988) 197–224, http://dx.doi.org/10.1016/0045-7825(88)90086-2.

[2] A. Bandyopadhyay, B. Heer, Additive manufacturing of multi-material structures, Mater. Sci. Eng. R 129 (2018) 1–16, http://dx.doi.org/10.1016/j.mser.2018.04.001.

[3] A.T. Gaynor, N.A. Meisel, C.B. Williams, J.K. Guest, Multiple-material topology optimization of compliant mechanisms created via polyJet three-dimensional printing, J. Manuf. Sci. Eng. 136 (6) (2014) http://dx.doi.org/10.1115/1.4028439, 061015.

[4] R. Sivapuram, P.D. Dunning, H.A. Kim, Simultaneous material and structural optimization by multiscale topology optimization, Struct. Multidiscip. Optim. 54 (5) (2016) 1267–1281, http://dx.doi.org/10.1007/s00158-016-1519-x.

[5] A. Pizzolato, A. Sharma, K. Maute, A. Sciacovelli, V. Verda, Multi-scale topology optimization of multi-material structures with controllable geometric complexity — Applications to heat transfer problems, Comput. Methods Appl. Mech. Engrg. 357 (2019) 112552, http://dx.doi.org/10.1016/j.cma.2019.07.021.

[6] O. Sigmund, S. Torquato, Design of materials with extreme thermal expansion using a three-phase topology optimization method, J. Mech. Phys. Solids 45 (6) (1997) 1037–1067, http://dx.doi.org/10.1016/S0022-5096(96)00114-7.

[7] L.V. Gibiansky, O. Sigmund, Multiphase composites with extremal bulk modulus, J. Mech. Phys. Solids 48 (3) (2000) 461–498, http://dx.doi.org/10.1016/S0022-5096(99)00043-5.

[8] O. Sigmund, A 99 line topology optimization code written in MATLAB, Struct. Multidiscip. Optim. 21 (2001) 120–127.

[9] T. Gao, W. Zhang, A mass constraint formulation for structural topology optimization with multiphase materials, Internat. J. Numer. Methods Engrg. 88 (8) (2011) 774–796, http://dx.doi.org/10.1002/nme.3197.
[10] D. Fujii, B.C. Chen, N. Kikuchi, Composite material design of two-dimensional structures using the homogenization design method, Internat. J. Numer. Methods Engrg. 50 (9) (2001) 2031–2051, http://dx.doi.org/10.1002/nme.105, URL https://onlinelibrary.wiley.com/doi/abs/10.1002/nme.105.
[11] O. Sigmund, Design of multiphysics actuators using topology optimization – part II: Two-material structures, Comput. Methods Appl. Mech. Engrg. 190 (49) (2001) 6605–6627, http://dx.doi.org/10.1016/S0045-7825(01)00252-3.
[12] L. Yin, G.K. Ananthasuresh, Topology optimization of compliant mechanisms with multiple materials using a peak function material interpolation scheme, Struct. Multidiscip. Optim. 23 (1) (2001) 49–62, http://dx.doi.org/10.1007/s00158-001-0165-z.
[13] M.Y. Wang, X. Wang, "Color" level sets: a multi-phase method for structural topology optimization with multiple materials, Comput. Methods Appl. Mech. Engrg. 193 (6) (2004) 469–496, http://dx.doi.org/10.1016/j.cma.2003.10.008.
[14] M.Y. Wang, S. Chen, X. Wang, Y. Mei, Design of multimaterial compliant mechanisms using level-set methods, J. Mech. Des. 127 (5) (2005) 941–956, http://dx.doi.org/10.1115/1.1909206.
[15] Z. Luo, L. Tong, J. Luo, P. Wei, M.Y. Wang, Design of piezoelectric actuators using a multiphase level set method of piecewise constants, J. Comput. Phys. 228 (7) (2009) 2643–2659, http://dx.doi.org/10.1016/j.jcp.2008.12.019.
[16] J. Stegmann, E. Lund, Discrete material optimization of general composite shell structures, Internat. J. Numer. Methods Engrg. 62 (14) (2005) 2009–2027, http://dx.doi.org/10.1002/nme.1259.
[17] E. Lund, Buckling topology optimization of laminated multi-material composite shell structures, Compos. Struct. 91 (2) (2009) 158–167, http://dx.doi.org/10.1016/j.compstruct.2009.04.046.
[18] T. Gao, P. Xu, W. Zhang, Topology optimization of thermo-elastic structures with multiple materials under mass constraint, Comput. Struct. 173 (2016) 150–160, http://dx.doi.org/10.1016/j.compstruc.2016.06.002.
[19] W. Zuo, K. Saitou, Multi-material topology optimization using ordered SIMP interpolation, Struct. Multidiscip. Optim. 55 (2) (2017) 477–491, http://dx.doi.org/10.1007/s00158-016-1513-3.
[20] X. Huang, Y.M. Xie, Bi-directional evolutionary topology optimization of continuum structures with one or multiple materials, Comput. Mech. 43 (3) (2008) 393–401, http://dx.doi.org/10.1007/s00466-008-0312-0.
[21] Y. Zheng, D. Da, H. Li, M. Xiao, L. Gao, Robust topology optimization for multi-material structures under interval uncertainty, Appl. Math. Model. 78 (2020) 627–647, http://dx.doi.org/10.1016/j.apm.2019.10.019.
[22] R. Sivapuram, R. Picelli, Topology optimization of binary structures using integer linear programming, Finite Elem. Anal. Des. 139 (2018) 49–61, http://dx.doi.org/10.1016/j.finel.2017.10.006.
[23] R. Sivapuram, R. Picelli, Y.M. Xie, Topology optimization of binary microstructures involving various non-volume constraints, Comput. Mater. Sci. 154 (2018) 405–425, http://dx.doi.org/10.1016/j.commatsci.2018.08.008.
[24] E.D. Sanders, A. Pereira, M.A. Aguiló, G.H. Paulino, An improved soft-kill BESO algorithm for optimal distribution of single or multiple material phases, Struct. Multidiscip. Optim. 58 (6) (2018) 2727–2759, http://dx.doi.org/10.1007/s00158-018-2094-0.
[25] O.G.-L. no, L. Mirabella, L. Dalloro, G.H. Paulino, Multi-material thermomechanical topology optimization with applications to additive manufacturing: Design of main composite part and its support structure, Comput. Methods Appl. Mech. Engrg. 363 (2020) 112812, http://dx.doi.org/10.1016/j.cma.2019.112812.
[26] W. Zhang, J. Song, J. Zhou, Z. Du, Y. Zhu, Z. Sun, X. Guo, Topology optimization with multiple materials via moving morphable component (MMC) method, Internat. J. Numer. Methods Engrg. 113 (11) (2018) 1653–1675, http://dx.doi.org/10.1002/nme.5714.
[27] O. Sigmund, Morphology-based black and white filters for topology optimization, Struct. Multidiscip. Optim. 33 (4) (2007) 401–424, http://dx.doi.org/10.1007/s00158-006-0087-x.
[28] F. Wang, B.S. Lazarov, O. Sigmund, On projection methods, convergence and robust formulations in topology optimization, Struct. Multidiscip. Optim. 43 (6) (2011) 767–784, http://dx.doi.org/10.1007/s00158-010-0602-y.
[29] A. Kawamoto, T. Matsumori, S. Yamasaki, T. Nomura, T. Kondoh, S. Nishiwaki, Heaviside projection based topology optimization by a PDE-filtered scalar function, Struct. Multidiscip. Optim. 44 (1) (2011) 19–24, http://dx.doi.org/10.1007/s00158-010-0562-2.
[30] Q. Xia, M.Y. Wang, Topology optimization of thermoelastic structures using level set method, Struct. Multidiscip. Optim. 42 (6) (2017) 837–857, http://dx.doi.org/10.1007/s00466-008-0287-x.
[31] S. Chu, M. Xiao, L. Gao, H. Li, J. Zhang, X. Zhang, Topology optimization of multi-material structures with graded interfaces, Comput. Methods Appl. Mech. Engrg. 346 (2019) 1096–1117, http://dx.doi.org/10.1016/j.cma.2018.09.040.
[32] G. Allaire, F. Jouve, A.-M. Toader, A level-set method for shape optimization, C. R. Math. 334 (12) (2002) 1125–1130, http://dx.doi.org/10.1016/S1631-073X(02)02412-3.
[33] M.Y. Wang, X. Wang, D. Guo, A level set method for structural topology optimization, Comput. Methods Appl. Mech. Engrg. 192 (1) (2003) 227–246, http://dx.doi.org/10.1016/S0045-7825(02)00559-5.
[34] G. Allaire, F. de Gournay, F. Jouve, A. Toader, Structural optimization using topological and shape sensitivity via a level set method, Control Cybernet. 34 (2005) 59–80.
[35] M. Bruyneel, P. Duysinx, Note on topology optimization of continuum structures including self-weight, Struct. Multidiscip. Optim. 29 (4) (2005) 245–256, http://dx.doi.org/10.1007/s00158-004-0484-y.
[36] P.D. Dunning, H. Alicia Kim, A new hole insertion method for level set based structural topology optimization, Internat. J. Numer. Methods Engrg. 93 (1) (2013) 118–134, http://dx.doi.org/10.1002/nme.4384.
[37] Q. Xia, T. Shi, L. Xia, Stable hole nucleation in level set based topology optimization by using the material removal scheme of BESO, Comput. Methods Appl. Mech. Engrg. 343 (2019) 438–452, http://dx.doi.org/10.1016/j.cma.2018.09.002.
[38] O. Querin, G.P. Steven, Y.M. Xie, Evolutionary structural optimisation (ESO) using a bidirectional algorithm, Eng. Comput. (Bradf.) (1998).

[39] X. Huang, Y. Xie, Convergent and mesh-independent solutions for the bi-directional evolutionary structural optimization method, Finite Elem. Anal. Des. 43 (14) (2007) 1039–1049, http://dx.doi.org/10.1016/j.finel.2007.06.006.
[40] G.I.N. Rozvany, A critical review of established methods of structural topology optimization, Struct. Multidiscip. Optim. 37 (3) (2009) 217–237, http://dx.doi.org/10.1007/s00158-007-0217-0.
[41] A.L. Rubèn, O.M. Querin, A.G. Jiménez, C.A. Gordoa, A sequential element rejection and admission (SERA) topology optimization code written in Matlab, Struct. Multidiscip. Optim. 58 (3) (2018) 1297–1310, http://dx.doi.org/10.1007/s00158-018-1939-x.
[42] D. Gao, in: D. Gao, V. Latorre, N. Ruan (Eds.), Canonical Duality Theory - Unified Methodology for Multidisciplinary Study, Springer International Publishing, Cham, 2017, pp. 263–276, http://dx.doi.org/10.1007/978-3-319-58017-3.
[43] D.Y. Gao, On topology optimization and canonical duality method, Comput. Methods Appl. Mech. Engrg. 341 (2018) 249–277, http://dx.doi.org/10.1016/j.cma.2018.06.027.
[44] Y. Liang, G. Cheng, Topology optimization via sequential integer programming and Canonical relaxation algorithm, Comput. Methods Appl. Mech. Engrg. 348 (2019) 64–96, http://dx.doi.org/10.1016/j.cma.2018.10.050.
[45] Y. Liang, G. Cheng, Further elaborations on topology optimization via sequential integer programming and Canonical relaxation algorithm and 128-line MATLAB code, Struct. Multidiscip. Optim. 61 (1) (2020) 411–431, http://dx.doi.org/10.1007/s00158-019-02396-3.
[46] D. Gao, in: V.K. Singh, D. Gao, A. Fischer (Eds.), Advances in Mathematical Methods and High Performance Computing, Springer International Publishing, Cham, 2019, pp. 3–50, http://dx.doi.org/10.1007/978-3-030-02487-1_1.
[47] D.Y. Gao, Canonical duality theory and algorithm for solving bilevel knapsack problems with applications, IEEE Trans. Syst. Man Cybern. Syst. 51 (2021) 893–904.
[48] R. Picelli, R. Sivapuram, Solving topology optimization with 0, 1 design variables and mathematical programming: the TOBS method, in: ProceEdings of the 13th World Congress of Structural and Multidisciplinary Optimization, WCSMO-13, Beijing, China, 2019.
[49] R. Picelli, S. Ranjbarzadeh, R. Sivapuram, R.S. Gioria, E.C.N. Silva, Topology optimization of binary structures under design-dependent fluid-structure interaction loads, Struct. Multidiscip. Optim. (2020) http://dx.doi.org/10.1007/s00158-020-02598-0.
[50] R. Sivapuram, R. Picelli, Topology design of binary structures subjected to design-dependent thermal expansion and fluid pressure loads, Struct. Multidiscip. Optim. 61 (2020) 1877–1895, http://dx.doi.org/10.1007/s00158-019-02443-z.
[51] R. Picelli, R. Sivapuram, Y.M. Xie, A 101-line MATLAB code for topology optimization using binary variables and integer programming, Struct. Multidiscip. Optim. accepted (2020).
[52] M.P. Bendsøe, O. Sigmund, Material interpolation schemes in topology optimization, Arch. Appl. Mech. 69 (9) (1999) 635–654, http://dx.doi.org/10.1007/s004190050248.
[53] B.-C. Chen, N. Kikuchi, Topology optimization with design-dependent loads, Finite Elem. Anal. Des. 37 (1) (2001) 57–70, http://dx.doi.org/10.1016/S0168-874X(00)00021-4.
[54] O. Sigmund, J. Petersson, Numerical instabilities in topology optimization: A survey on procedures dealing with checkerboards, mesh-dependencies and local minima, Struct. Multidiscip. Optim. 16 (1) (1998) 68–75, http://dx.doi.org/10.1007/BF01214002z.
[55] D. Li, I.Y. Kim, Multi-material topology optimization for practical lightweight design, Struct. Multidiscip. Optim. 58 (3) (2018) 1081–1094, http://dx.doi.org/10.1007/s00158-018-1953-z.